CZECH TECHNICAL UNIVERSITY
IN PRAGUE

Faculty of Nuclear Sciences and Physical Engineering

Department of Physics

Research Topic

Application of semiconductor detectors in fusion experiments

Bc. Peter Švihra

Supervisor: Ing. Michal Marčišovský, PhD.

Prague, 2017

ČESKÉ VYSOKÉ UČENÍ TECHNICKÉ
V PRAZE
Fakulta Jaderná a Fyzikálně Inženýrská
Katedra fyziky

Výzkumný úkol

Použití polovodičových detektorů ve fúzních experimentech

Bc. Peter Švihra

Vedoucí práce: Ing. Michal Marčišovský, PhD.

Praha, 2017

Declaration

I hereby declare, that I've written this thesis by myself and I've used only the materials stated in the references section.

I have no reason to object to use this work according to the section 60 of Act No. 121/2000 Coll.,On Copyright, on Rights Related to Copyright, and on Change of Some Acts (Copyright Act)

Prague, date ....

Peter Švihra

Acknowledgement

Thesis title:
Application of semiconductor detectors in fusion experiments

Author: Bc. Peter Švihra

Field of study: Physics and Technology of Thermonuclear Fusion

Thesis type: Research topic

Supervisor: Ing. Michal Marčišovský, PhD.

Abstract:
Due to the plasma properties, discharges in the devices tend to undergo a rapid termination - disruption. These processes are unwanted, causing problems in achieving high fusion yield or potentially damaging the instrumentation.

For the pinches or plasma foci, the disruptions are usually caused by a number of instabilities.

In the tokamaks, a by–product of such process can result in creation of a population of electrons accelerated to high energies. These so–called runaway electrons then behave as if in the particle accelerator and can cause damage to the vacuum vessel and other critical components.

Since the disruptions tend to generate radiation, new diagnostic methods, such as usage of semiconductor pixel detectors, are necessary. In order to properly operate such detectors, different calibration processes have to be performed. As a result, good spatial and temporal resolution can be obtained, resulting in acquisition of relevant information about the runaway electrons or development of the instabilities. This is crucial for the further advancements of the fusion research.

Results of the measurements from different experiments are promising, however, for the proper interpretation further analysis and simulations of the whole experiments should be made.

Keywords: plasma, plasma focus, instabilities, PFZ-200, tokamak, runaway electrons, GOLEM, COMPASS, semiconductor pixel detector, Medipix2, ASPIRE, CoaXPress, Timepix3, SPIDR

Contents

List of Figures

Introduction

Since the thermonuclear fusion is considered a future energy source, lot of different devices were created in order to achieve conditions resulting in creation of more energy than was consumed. This ranged from small table-sized experiments up to large ones currently being tested or developed.

One of the first types were pinches, simple wires which are heated and compressed by large electric currents and magnetic field. The configuration works in pulses only and is a subject to emergence of different magnetohydrodynamic plasma instabilities. After a long research, it was shown that even with scaling, the device is not capable of generating large fusion yield. However, it proved to be good for research of instabilities, different diagnostics techniques and it can be used as an X-ray or neutron source.

On the other hand, tokamaks (from Russian toroidal'naya kamera s magnitnymi katushkami – toroidal chamber with magnetic coils) are devices more complex to construct, showing promising results for being an operational fusion reactor. They are using electromagnetic induction, microwaves, accelerated neutral atoms or their combination to heat and ionize gas. The confinement is provided by the magnetic field, generated by the coils around the toroidally-shaped chamber, together with the field created by induced electric current in the plasma. By this process, particles receive necessary kinetic energy for thermonuclear fusion - typically a deuterium–tritium reaction, which produces helium and a neutron. For a typical tokamak plasma density, the confinement time falls within the range of a few seconds and can be terminated by disruptions.

One of the possible outcomes of a disruption is generation of electrons with high energy – so called runaway electrons (RE). Their generation at a large tokamaks can cause damage to the vacuum vessel, as is shown in the figure 1. The worst case scenario is a perforation of the vacuum vessel.

Since the RE process is still not well understood, new diagnostic methods are necessary, providing information about time and position of impact of an electron beam. Semiconductor detectors are widely used in high energy physics (HEP) as particle tracking detectors - due to their sensitivity to ionizing radiation. They can also be successfully applied in new system for plasma diagnostic applications.

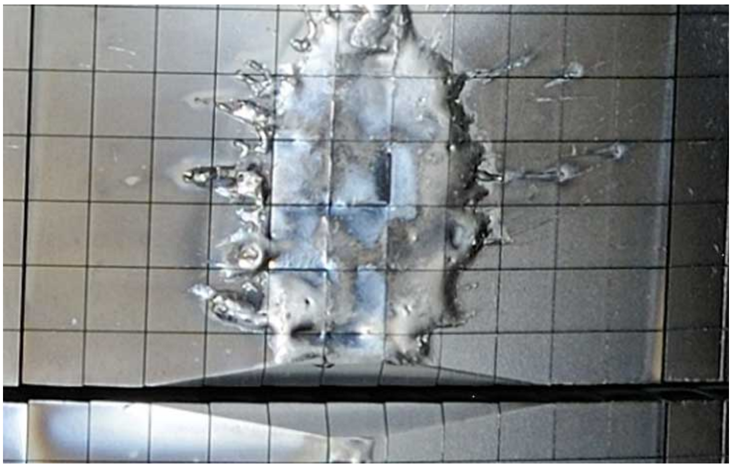

Figure 1: Re-deposited molten beryllium appears on tiles inside the JET vessel after experiments focused on RE generation and effects. [4]

Chapter 1

Fusion Devices

There are several approaches of studying plasma and fusion in particular. For obtaining more energy than is consumed, Lawson derived a simple criterion

$$n\tau \geq \frac{3k_BT}{\frac{\eta}{4(1-\eta)}\left\langle\sigma v\right\rangle \Delta E - \alpha T^{\frac{1}{2}}}, \tag{1.0.0.1}$$

where n is the density of plasma, τ is containment time, η is the efficiency factor, ΔE is the total energy output and α is a constant related to the radiation power loss. For D–T fusion, the Lawson's criterion is $n\tau \geq 10^{14}$ cm^{-3}s. [5]

As is easily derived from formula mentioned above, for a large confinement time τ, plasma density n can be smaller and vice–versa. These boundary values can be achieved in magnetic ($n \sim 10^{14}$ cm^{-3}, $\tau \sim 1$ s), or inertial confinement ($n \sim 10^{23}$ cm^{-3}, $\tau \sim 10^{-9}$ s). Fusion experiments with low plasma density such as tokamaks, spheromaks and stellarators belong to the magnetic confinement category, whereas laser driven fusion is a type of the inertial confinement. Pinches and plasma foci fit with their parameters ($n \sim 10^{18}$ cm^{-3}, $\tau \sim 10^{-4}$ s) somewhere in between.

Moreover, such devices are used for elementary plasma research. They will help understanding and further development of an operational fusion reactor.

1.1 Plasma Focus

Using a coaxial configuration of electrodes, i.e. large anode in the center surrounded by smaller cathodes on the circular periphery, the ionized gas can be accelerated thus creating focused plasma on top of the anode.

At the top a Z-pinch effect occurs, in which the current flows in the same direction as the column is formed, creating poloidal magnetic field. Comparing thermal pressure p to magnetic pressure $B^2/2\mu_0$ gives parameter β, defined as

$$\beta = \frac{p}{\frac{B^2}{2\mu_0}}. \tag{1.1.0.1}$$

For pinches $\beta \approx 1$ thus the kinetic and magnetic forces in the pinch are in equilibrium. However, even for such configuration instabilities occur, as is described in the next chapter.

1.1.1 Description

There are two different construction types of plasma foci – Mather (USA) and Filippov (USSR). The difference between them is in the ratio of diameter d to length z of inner

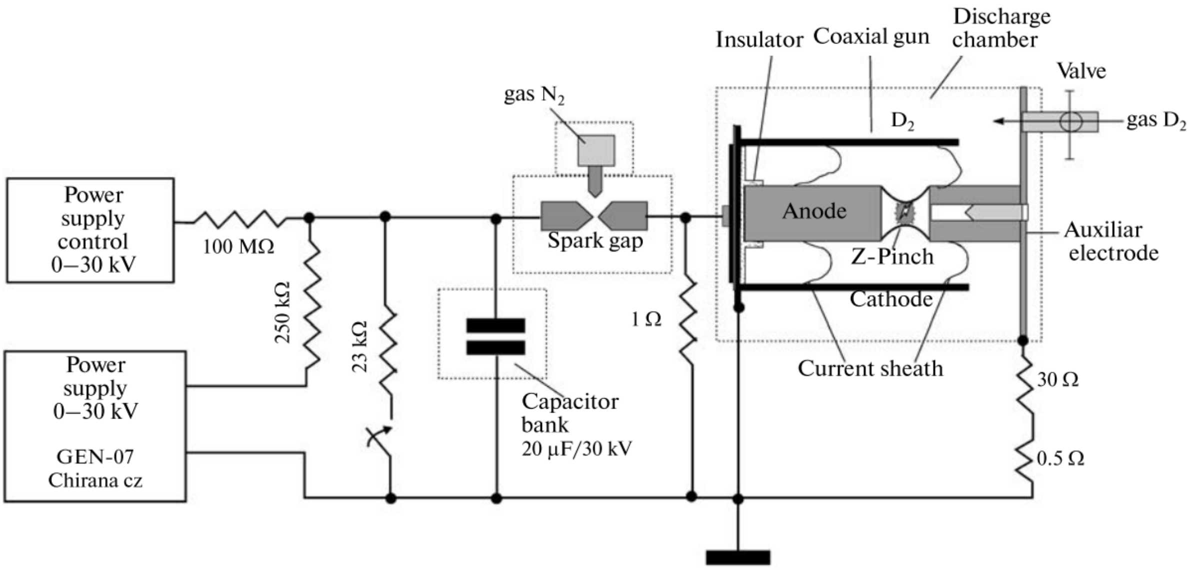

Figure 1.1: A scheme of a plasma focus with an equivalent electronic circuit. The capacitor bank is discharged via spark gap. Discharge in gas begins over an insulator, continues accelerated to the top where is focused on the anode. [7]

electrode. For Mather type, $d/z < 1$; for Filippov, $d/z > 1$ [6]. Nowadays, Mather type is used more often.

The process of formation of the focus can be divided into three main phases as is in the figure (1.1) and furtherly explained.

I. Breakdown phase According to the Paschen's law, the breakdown voltage is a function of the pressure p and the gap distance d between the electrodes

$$V_b = \frac{Bpd}{\ln Apd - \ln\Big(\ln\big(1 + 1/\gamma_{se}\big)\Big)}, \tag{1.1.1.1}$$

where A, B are empirically measured constants dependent on the materials and $\gamma_{\rm se}$ is the secondary electron emission coefficient [8]. When this voltage is applied to the electrodes, the gas above the insulator is ionized. Current starts to flow through the created plasma layer, generating a magnetic field. Due to the Lorentz force, plasma is accelerated firstly in the radial direction to the cathodes, later when the discharge reaches anode, it is accelerated in the axial direction. This process is shown in figure (1.2), it is called the inverse pinch – the magnetic forces affect the plasma sheath to expand instead of pinch. [9].

II.–III. Acceleration phase Phase begins at the end of the breakdown phase, when plasma connects cathode and anode. The axial magnetic force $\mathbf{j_r} \times \mathbf{B}_\theta$ depends on the radius as $1/r$, therefore, the velocity of the plasma sheath is larger near the central anode. However, the accumulation of the plasma mass is non–linear: the mass build–up near the central electrode is linear, but drops in the direction towards the outer electrodes, where it is almost non–existent. This is called "snow–plow" effect, which slows down the movement of the central plasma sheath. [9]

IV. Collapse phase When leaving the conical arrangement of the electrodes, the plasma sheath is focused on the top of the anode. The compressed part of plasma then be-

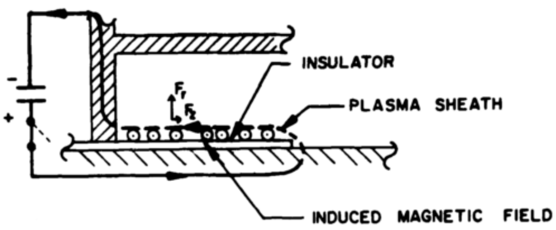

(a) Ionization of gas over an insulator, start of current flow.

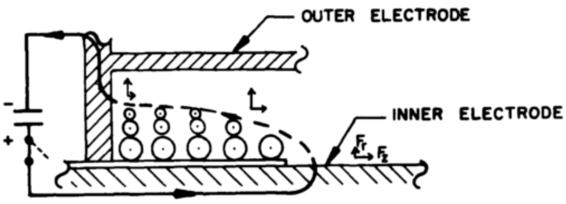

(b) Acceleration of plasma layer in radial direction via Lorentz force.

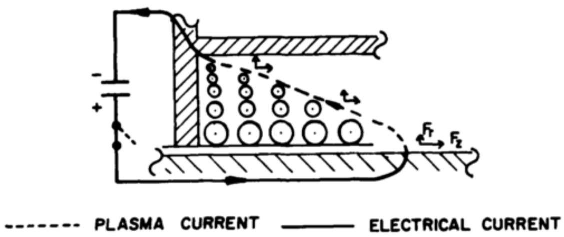

(c) Acceleration of plasma in axial direction.

Figure 1.2: Breakdown phase (inverse pinch effect) of plasma focus. [9]

haves in a similar fashion to z–pinch, generating X–rays and fusion neutrons, considering an application of the proper filling gas. The instabilities are also analogical.

1.1.2 PFZ-200

Plasma focus PFZ-200 is an experimental device located at the Faculty of Electrical Engineering, Czech Technical University (FEE CTU) in Prague. It is a small plasma focus, convenient for testing different electrode configurations, loads and diagnostic tools. [7]

Schematics of the device is shown in figure (1.1). Configuration is of Mather type, with dimensions of the central electrode 2.5 cm in diameter and 11 cm in length. Electrode is made of CuW and is connected as an anode, an insulator is made of Al_2O_3. It reaches 35 mm from the bottom. Outer electrodes are from steel, 6 mm in diameter and 19 cm long. The experiment has 12 of these cathodes, coaxially arranged with diameter of cylindrical configuration 6 cm. Against the central anode with gap between 1 cm to 2 cm an auxiliary Cu electrode with the diameter of 2.7 cm can be placed. This electrode supports pinching of the plasma, although during experiment auxiliary electrode was not used. [7]

The vacuum is maintained by a combination of turbo–molecular and rotary pumps. The vacuum vessel is then filled with Deuterium gas ${}^2_1D$ at pressure in the range of 200 Pa to 300 Pa. Four capacitor banks have total stored energy 5.2 kJ and are charged to voltage $U_0 = 15\,\mathrm{kV}$, which allows maximal current in deuterium $I \approx 250\,\mathrm{kA}$, during 2 µs interval. The discharge occurs when air filled spark gap triggers. Shots can be repeated every 5 minutes.

1.2 Tokamak

Standard tokamak configuration is a toroidal vacuum vessel, possibly in a more advanced D-shaped geometry. The vessel is surrounded by toroidal and poloidal magnets, providing

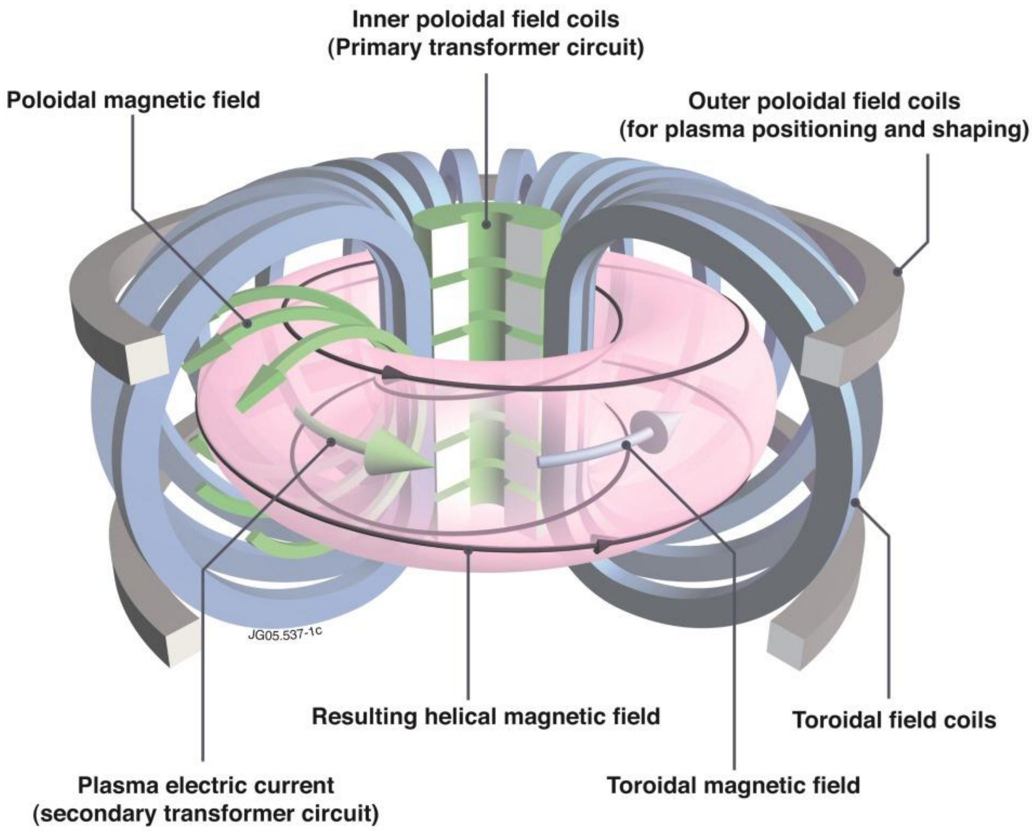

Figure 1.3: Schematic of a tokamak device, basic process of plasma containment using combination of toroidal and poloidal magnetic field. [1]

field for confinement of plasma. This simplified geometry is shown in the figure 1.3. Moreover, different tools for diagnostics and plasma heating are positioned all around the torus.

Currently, the largest experiment, called ITER, (from Latin *iter* – direction, way) is being built in Cadarache, France. There are many more tokamaks around the world, two of the in Prague, Czech Republic – oldest operational tokamak GOLEM and medium-sized tokamak COMPASS.

1.2.1 Description

For the easy description of the tokamaks, toroidal geometry is used with toroidal direction φ (following the torus), poloidal direction θ (perpendicural to toroidal) and radial direction. For correct description of position, two radii are used: major radius R_0, describing size of the torus from the middle to the centre of the vessel (so called magnetic axis), and minor radius a, describing size of the poloidal crossection.

The coils usually generate toroidal field of the order of 1 T. One of the important parameters is β which compares plasma pressure p to the pressure of magnetic field B, similarly to the Z-pinch (see equation (1.1.0.1)). However, for the tokamak combination of both toroidal and poloidal fields is included.

To achieve the creation of helical magnetic field and ohmic heating, a current I_p is induced in plasma. For that purpose, a transformer in the middle of the tokamak is needed where plasma serves as the secondary winding. The downside of such effect is that the current in the primary winding must be increasing and that is impossible to achieve for long time periods. Moreover, the resistance of plasma is decreasing with higher temperatures, however, methods of additional heating have been developed, such as neutral beam injection or heating via electromagnetic waves - most commonly resonance for electron and ion cyclotron frequencies.

The before mentioned helical magnetic field consists of toroidal field from coils and poloidal magnetic field created by induced current according to Ampére's law. The fraction of poloidal to toroidal field is best described by the safety factor q. It compares the number of rotations needed in toroidal direction, to achieve one rotation in poloidal direction. Typical tokamak values have up to $q \approx 3$ at the edge, as larger values lead to instabilities. [1] The ideal safety factor would be imaginary, meaning that the field lines would never connect.

Plasma confined in the torus tends to expand, therefore additional poloidal coils are used to help shape the plasma (see fig. 1.3). Different diagnostic systems are used for feedback, enabling on-flight calculation of needed generated field to help contain the plasma.

The shape of the vessel was circular at first, however, it was later changed to a D-shape. This was due to plasma having more particles in a stronger magnetic field, since the intensity of the magnetic field decreases as $1/r$, the middle of the torus represents so called high field side (HFS) and the outer part is low field side (LFS). Furthermore, toroidal coils constructed this way are sturdier.

Another main concern with tokamaks is interaction of plasma with the walls of the vacuum vessel. By interacting, the vessel material can enter the plasma and contaminate it, causing energy losses and worsening the plasma parameters. The last surface with enclosed magnetic field lines is called last closed flux surface (LCFS), outside of which is scrape-off layer (SOL). Studies of SOL are important due to the interactions of plasma and disruptions with wall. At the beginning, a simple construction with limiter (obstacle limiting the plasma radius) was used, later changed to the divertor construction (plasma separated to specific region all around the torus). The divertor configuration includes X-point - point where $B_\theta = 0$. Usage of such construction lead to H-mode, in which the plasma has larger temperature and stability. Comparison of the two types is in the figure 1.4.

1.2.2 GOLEM

The tokamak GOLEM is an education-oriented tokamak located at the Faculty of Nuclear Sciences and Physical Engineering (FNSPE) at CTU in Prague.

Its major radius is $R_0 = 0.4\,\mathrm{m}$ and minor radius $a = 0.1\,\mathrm{m}$. The typical toroidal field is $B_T \approx 0.4\,\mathrm{T}$ and plasma current in the flat-top phase $I_p \approx 5\,\mathrm{kA}$. The usual pulse length is $t \approx 20\,\mathrm{ms}$.

Energy is stored in the capacitor banks, charged prior to each discharge.

A unique features of this experiment are the possibility of a complete remote handling operation via a secure Internet access and a firing rate roughly 1 discharge per 2 minutes.

1.2.3 COMPASS

The COMPASS tokamak of the Institute of Plasma Physics of the Czech Academy of Sciences (IPP ASCR) in Prague, is a medium-size experimental fusion device with ITER-like plasma cross-section, major radius $R_0 = 0.56\,\mathrm{m}$ and minor radius $a = 0.23\,\mathrm{m}$. The

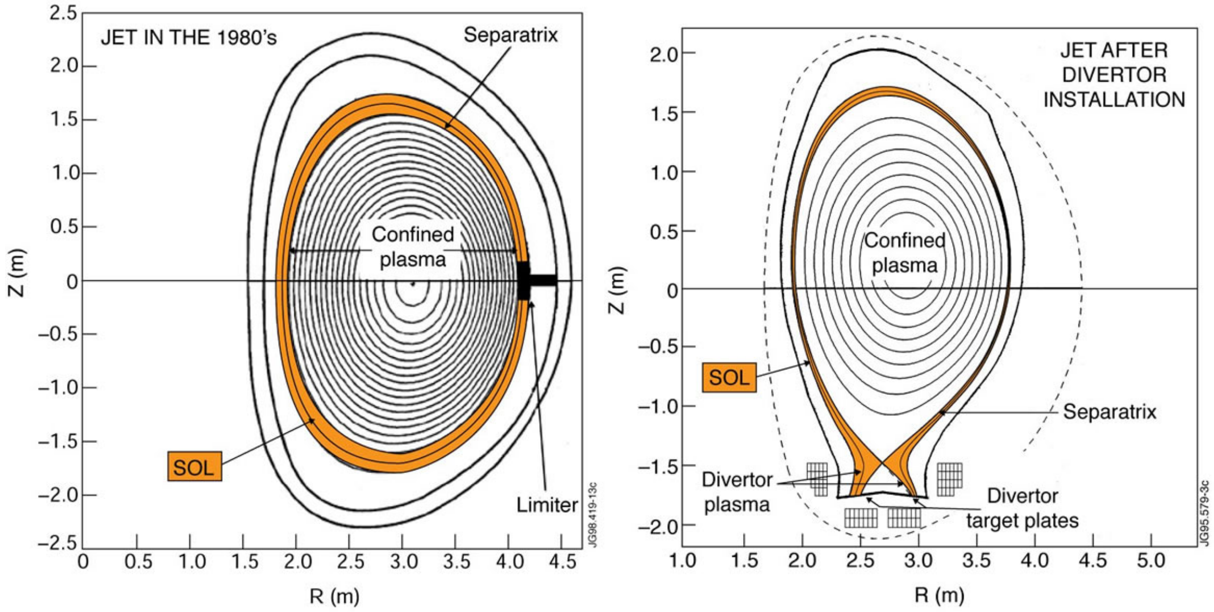

Figure 1.4: Comparison of limiter and divertor configuration of tokamak. Separatrix (last closed flux surface) and scrape-off layer (SOL) are highlighted. [4].

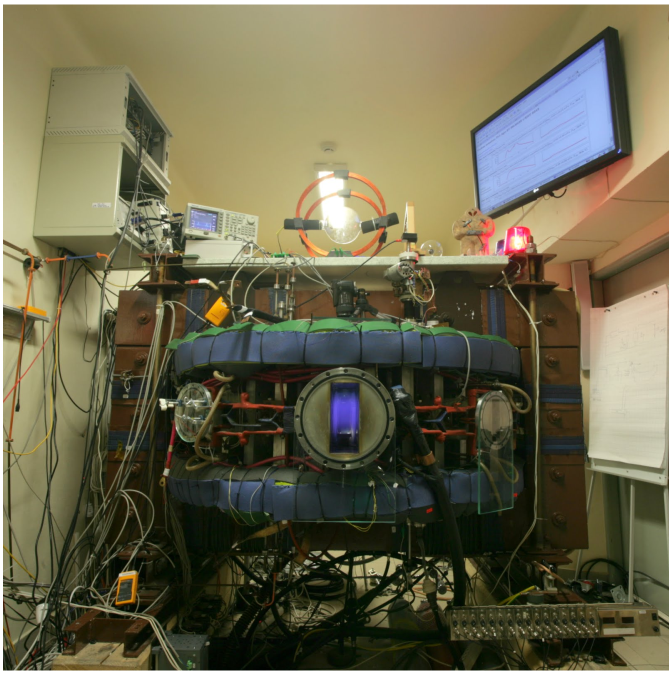

Figure 1.5: Image of tokamak GOLEM.

Figure 1.6: Image of tokamak COMPASS.

typical toroidal field is $B_T = 1.2\,\mathrm{T}$ and plasma current in the flat-top phase $I_p > 100\,\mathrm{kA}$. The usual pulse length is $t \approx$ hundreds ms.

As COMPASS is larger than GOLEM, energy needed for magnets and plasma heating is stored in a flywheel-generator, 45 MJs of power in total. Four AC/DC thyristors are then used as an interlink between the generator and tokamak. [10] The vacuum is pumped down to the range of $1 \cdot 10^{-6}\,\mathrm{Pa}$ to $3 \cdot 10^{-6}\,\mathrm{Pa}$ and operates with Deuterium gas. The system controls gas level during the discharge, enabling changes of plasma pressure and even injecting different types during the pulse, such as Argon. Before each operation, a glowing discharge is used in order to clean the chamber of adsorbed particles.

The COMPASS plasma can be operated in both limiter and divertor configuration, the latter allowing H-mode operation. [11] Therefore the tokamak is of ITER-type, highly relevant for current fusion research. Such configuration enables efficient plasma positioning via the usage of feedback system.

The experimental operation of the tokamak is mainly focused on plasma edge physics, runaway electrons, and development of diagnostic methods.

Chapter 2

Plasma Disruptions

Due to the intrinsic properties of plasma, disruptions such as hydrodynamic instabilities or other effects caused by collisions exist. These are unwanted processes, observed in all experimental devices and causing issues related to the plasma containment and device integrity.

2.1 Plasma Instabilities

The plasma instabilities can be divided into two categories according to their origin:

- **Hydrodynamic** are caused by macroscopic motions of the plasma, i.e. an electron two–stream instability.
- **Kinetic** are based on interaction of specific particles with unstable mode, like ion acoustic-drift instability.

However, the first category is more frequently the subject of studies in pinches and plasma foci. [6]

The hydrodynamic instabilities are applying perturbation theory of a wave–like form of the plasma flow. For equilibrium, the solution in cylindrical coordinates depends on the distance from z–axis. It can be therefore written as a static solution with perturbation

$$\psi(t, r, \varphi, z) = \psi_0(r) + \psi_1(r)\mathrm{e}^{\mathrm{i}m\theta + \mathrm{i}k_z z - \mathrm{i}\omega t}, \quad m = 0, \pm 1, \pm 2, \ldots \tag{2.1.0.1}$$

where $\psi_0(r)$ is the static solution, a disorder created from an aperiodic part $\psi_1(r)$, together with an oscillating exponential. Elements in the exponential are m modal number, θ azimuthal angle, k_z axial part of wave vector and ω angular frequency.

For the approximation of the plasma column with current flowing on the surface, in the direction of the column, the stable solution is described as

$$1 + \frac{m^2}{kr_0}\frac{K_m(kr_0)}{K'_m(kr_0)} > 0 \tag{2.1.0.2}$$

where m is modal number, K_m is modified Bessel function of the second kind, k is wave number and r_0 radius of the plasma column. This stability condition is called Kruskal - Safran. As the derivation of modified Bessel function is always negative, the equation can be rewritten to

$$F(x) = xK'_m(x) + m^2K_m(x) > 0, \tag{2.1.0.3}$$

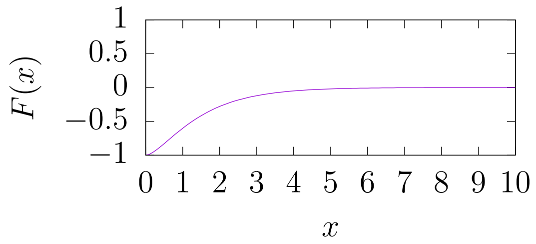

(a) $m = 0$.

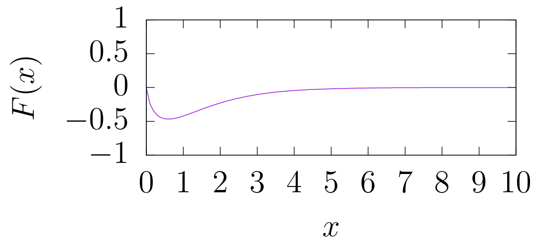

(b) $m = 1$.

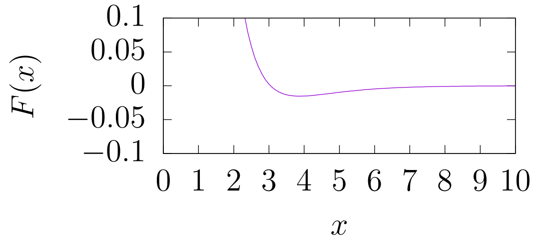

(c) $m = 2$.

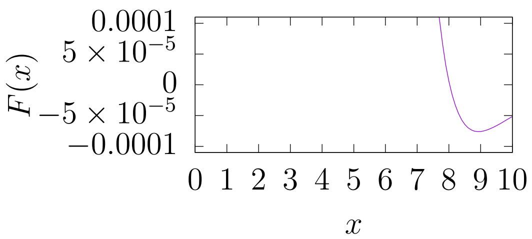

(d) $m = 3$.

Figure 2.1: Different modes of Kruskal-Safran instability according to the equation (2.1.0.3).

where $x \equiv kr_0$. As seen in the figures 2.1, the modes $m = 0$ and $m = 1$ are for such configuration always unstable. The stability could be enhanced by spiral magnetic field. [12]

Another hydrodynamic instabilities occur on the surface where parts of plasma with different parameters meet: Rayleigh–Taylor or Diocotron instability.

2.1.1 Sausage Instability

The shape of this instability corresponds to the equation (2.1.0.1) for $m = 0$. The locations where plasma is compressed and expanded are repetitive, and the total volume is preserved.

Being dependant on $1/r$, the azimuthal component of magnetic field B_θ is different in every point along the z–axis. Therefore in places where plasma is expanded, B_θ is smaller and where plasma is compressed B_θ is larger than in equilibrium. This causes an additional compression and expansion caused by magnetic field. The name "sausage" is derived from its shape, shown in figure (2.2).

This instability can be reduced by applying an axial magnetic field B_z, i.e. creating θ–z pinch. Those field lines are frozen in plasma, creating a force opposing to the change.

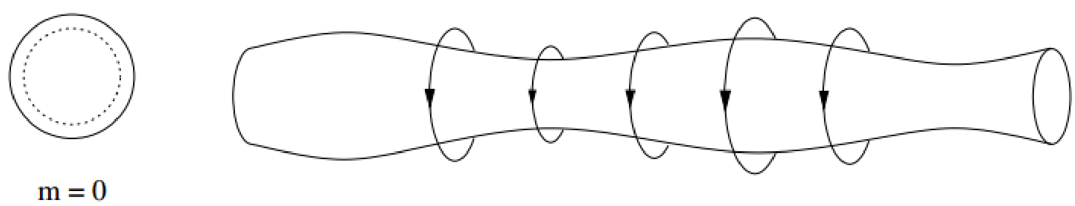

Figure 2.2: The physical form of sausage instability for z–pinch with cross–section where the dotted circle represents equilibrium. The magnetic field lines are represented by lines with arrows. [13]

2.1.2 Kink Instability

With $m = 1$ in the equation (2.1.0.1), the perturbation of the wave function results in the bending of the pinch. This bend causes the density of the lines of the magnetic field B_θ to get thicker on the concave and thinner on the convex side of the bend. As in the sausage instability, the arrangement of those lines enhances formation of the instability, creating kink, thence its name. It is shown in the figure (2.3).

Using an additional axial magnetic field, the pinch becomes more stable due to the pressure which is reacting to the changes in the density of the azimuthal field.

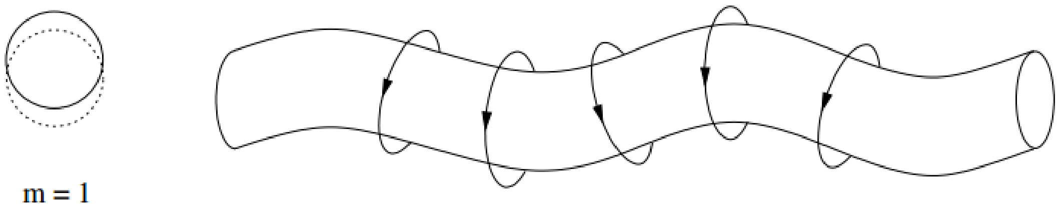

Figure 2.3: The physical form of kink instability for z–pinch with cross-section where the dotted circle represents equilibrium. The magnetic field lines are represented by lines with arrows. [13]

2.1.3 Hotspots

In the initial phase of the plasma column collapse, hotspots – structures with high density and temperature, occur. At first, they were considered elements created by the sausage instability; however, this has since been disproved. Those spots emit hard X–rays, neutrons, nonthermal electrons and ions with energies from 20 keV to 1 MeV, they are always preceded by electron–beam–excited characteristic lines. [6]

In the figure (2.4) a Schlieren photography of pinch of a wire in time is shown. The picture right represents the position of hotspots.

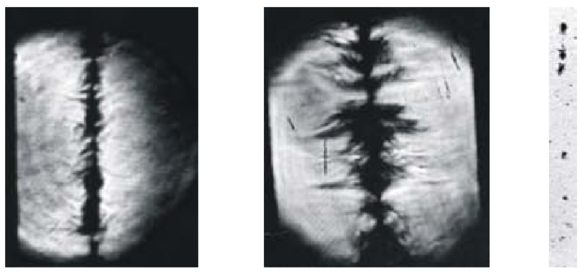

Figure 2.4: Schlieren photography of pinch of a wire with a diameter $r = 25$ μm, in times $t_1 = 14$ ns and $t_2 = 41$ ns, made in Imperial College in London, UK. In the right picture is an image of hotspots radiating in soft X–ray spectre. [14]

2.2 Runaway Electrons

The generation of RE happens when the acceleration caused by the electric field is larger than the opposing friction force. It can occur both in terrestrial, extraterrestrial or in artificial plasmas. An example of the process in nature is acceleration of electrons during thunderstorms. In tokamaks, this can happen when the intensity of the electric field is increased e.g. during loss of conductivity.

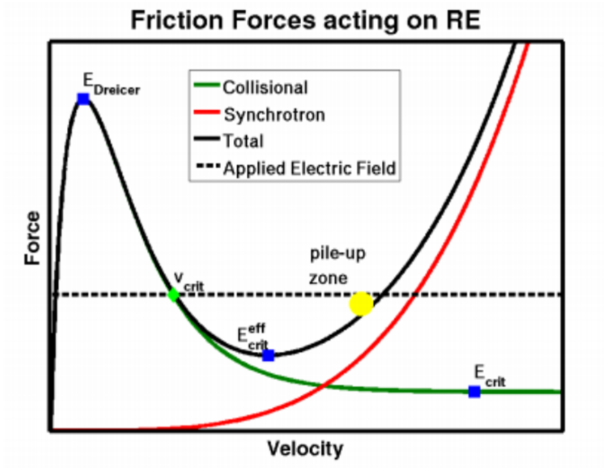

Figure 2.5: Friction force acting on electron depending on its velocity. Illustrated in arbitrary units according to [2].

2.2.1 Derivation

Equation describing the process is derived from Fokker-Planck equation [15] . For one dimensional example, the change in the momentum of electrons is described by:

$$\frac{\mathrm{d}}{\mathrm{d}t}(mv) = eE - C_e \psi(v/v_0) \tag{2.2.1.1}$$

$$\psi(x) \equiv \frac{2}{\sqrt{\pi}x^2} \int_0^x \xi^2 e^{-\xi^2} \mathrm{d}\xi, \tag{2.2.1.2}$$

where m is electron mass, v is standard and v_0 is thermal electron velocity, e elementary electric charge, E external electric field, C_e constant, $\psi(x)$ is Chandresekhar function.

The figure 2.5 shows dependency of a friction force on an electron velocity. It is a combination of collisional effects (Chandresekhar function) and radiative losses, compared to the accelerating electric force eE. When the friction force is larger than the electric force (up to v_{crit}), electrons are slowed. However, when velocity reaches the critical value, they are accelerated to a pile-up zone (and not further due to the deceleration caused by radiative processes). This process is still not well described as collisional effects are calculated for non-relativistic electrons only.

Moreover, the collisional force has its local maximum for small velocities in the form of Dreicer electric field E_{Dreicer} [15]

$$E_{\mathrm{Dreicer}} = \frac{n_e e^3}{4\pi\varepsilon_0^2 kT_e} \ln \Lambda. \tag{2.2.1.3}$$

If the intensity of electric field is larger than this value, RE are always generated.

2.2.2 Generation

Runaway electrons can be divided into two large groups - primary (generated by applied electric field) and secondary (mostly generated by interaction of primarily created RE with other electrons). The processes can be explained in detail on thermal Maxwellian distribution of electrons, plotted in velocity-space in figure 2.6.

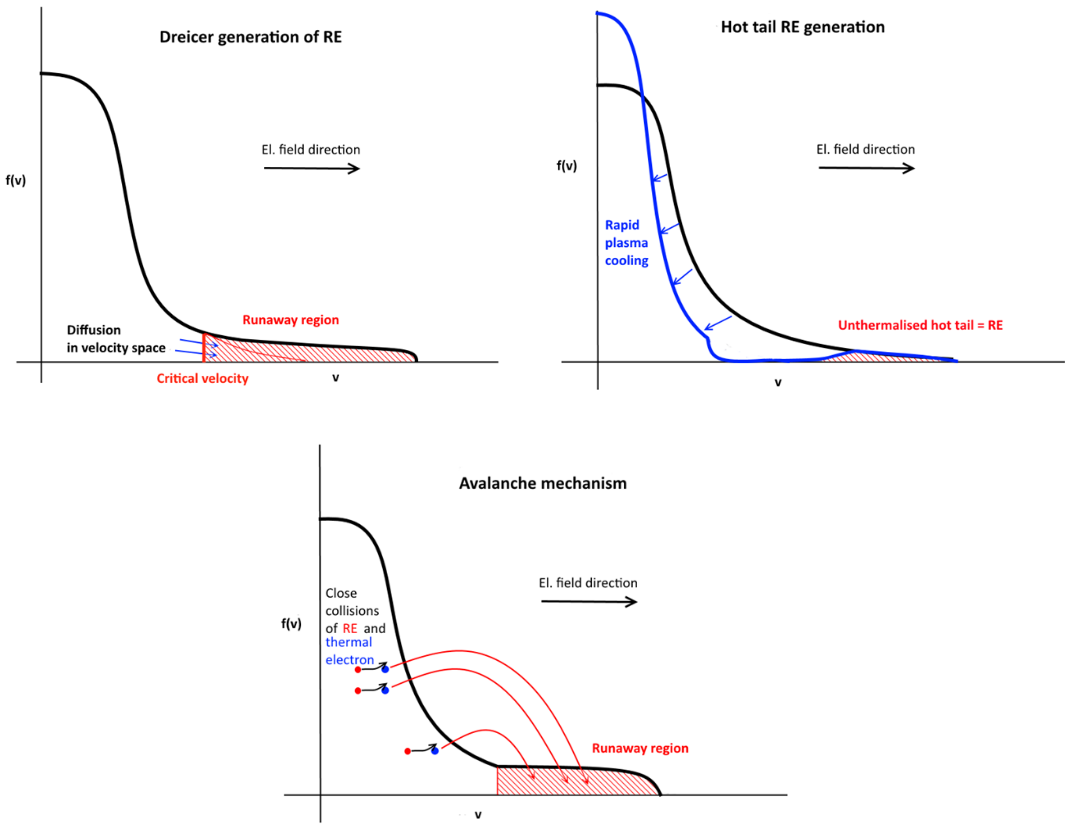

Figure 2.6: Types of generation processes of RE [3]. Upper left figure is classic Dreicer, upper right represents hot tail and lower avalanche mechanisms.

2.2.3 Primary RE

Dreicer The most basic type of RE generation is acceleration of electrons by electric field, as described in section 2.2.1. Due to the diffusion processes in the velocity distribution (figure 2.6 top), initially slower electrons can reach the critical velocity and be severely accelerated.

Hot tail When plasma is rapidly cooled by disruptions, velocity of the bulk of the electron is decreased. Since the cooling time of plasma is much shorter than the collisional time of the fastest electrons, they are not decelerated and remain in the hot tail. Moreover, as the temperature and conductivity decrease, intensity of an electric field is increased, which gives ideal conditions for RE generation.

Secondary RE

Avalanche The already created RE can interact with thermal electrons, transferring part of their energy, possibly large enough to get them into the runaway region.

Chapter 3

Semiconductor Pixel Detectors

Silicon semiconductor detectors are the most widely used type of the solid-state detectors in HEP. By doping silicon (or germanium) lattice with both donors (lithium, arsenic, phosphorus) and acceptors (boron, aluminium) of electrons, and combining two differently doped parts, a $p-n$ junction can be created. Around the junction, a depletion region emerges, which is sensitive to incoming ionizing radiation. The volume of this region can be increased by an applied reverse-bias voltage to the junction.

When incident ionizing particle passes through the sensor, electron-hole pairs are created in the depletion region and move along the electric field lines between $p-$ and $n-$ doped areas, in the opposite directions. These charges then arrive to the collecting electrodes where electric signal is formed and measured.

Such detectors can have detection channels in strip (sensitive lines) or pixel (sensitive matrix) configurations. Each of the detection elements (strips or pixels) is connected to an Application Specific Integrated Circuit (ASIC), in which a conversion from an analog pulse to a digital signal is performed. Readout of the detector is ensured by data acquisition system which provides communication to and from computer.

3.1 Interaction of Ionizing Radiation with Matter

Ionizing radiation is defined as a particle radiation with energy sufficient to ionize atoms. It can be formed as a by–product of nuclear reactions, produced in particle accelerators or generated in X–ray tubes. Ionizing radiation can be divided into two basic categories:

- Direct ionization, i.e. electrons and heavy charged particles. They ionize surrounding atoms directly by Coulomb interaction.
- Indirect ionization with neutral hadrons such as neutrons and electromagnetic radiation, where secondary charged particles ionize the surrounding environment by a direct interaction.

Particle detectors can only measure charged particles. Heavy charged particles and electrons interact primarily through Coulomb forces with electrons in the absorber, interactions with nuclei are rare. The incident particle is slowed down and, according to the law of conservation of momentum, liberated electrons are accelerated. This way, atoms in detector are ionized and pairs of electrons and positive ions or holes are created.

Having thousands of times larger mass than electrons, heavy charged particles ionize medium in the straight path. In comparison, incident electrons have large deviations in their path due to having the same mass as atomic electrons.

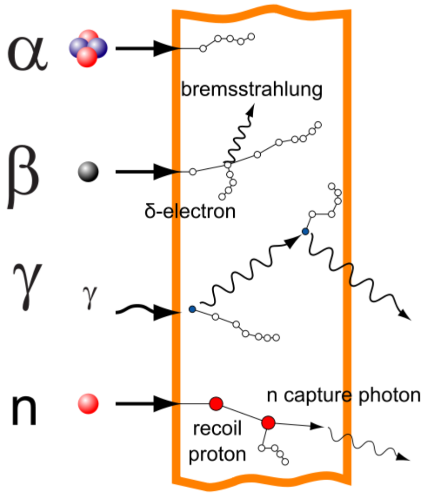

Figure 3.1: Interaction of ionizing radiation with matter.

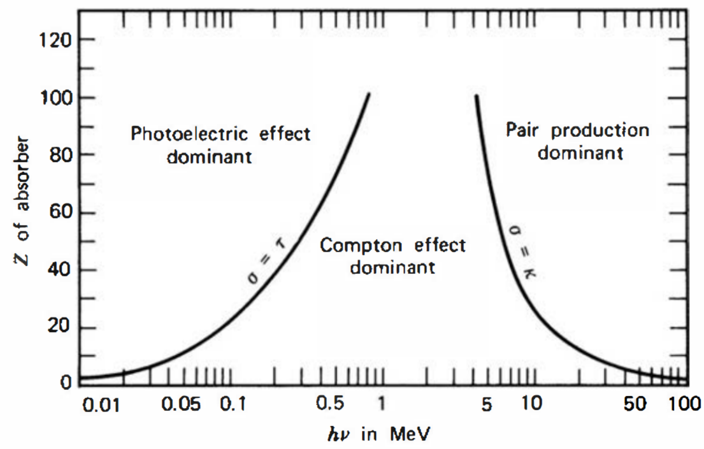

Figure 3.2: Dependence of photon–interaction processes on atomic number Z and energy $h\nu$. For silicon, photoelectric effect is dominant up to ≈ 70 MeV. [16]

In order to detect energetic photons or neutrons, the radiation must generally undergo catastrophic interaction – radically altering its properties. [16] For X– or gamma rays, it is a creation of secondary electrons, via the process of Compton scattering, photoelectric absorption or electron–positron pair creation, occurring at different energies. For neutrons, it is a creation of heavy charged particles, as a result of neutron–induced nuclear reactions or from gaining kinetic energy from collision. Products of these processes then interact as direct ionization mentioned above.

The measurements in this work were focused on the detection of X–rays, therefore the processes of their interaction are described in more detail. The figure 3.2 describes which processes occur in dependence on atomic number Z and different energies $h\nu$.

3.1.1 Photoelectric absorption

Incident photon undergoes an interaction with electron in atomic shell. Photon is absorbed and so called photoelectron is ejected from shell with kinetic energy E_{e^-}

$$E_{e^-} = h\nu - E_b, \tag{3.1.1.1}$$

where h is Planck constant, ν frequency of photon and E_b binding energy of electron. Therefore, photon must have energy greater than binding for reaction to occur.

3.1.2 Compton scattering

Incoming photon is deflected on an electron in the absorbing material, part of the energy is transferred to the electron. This results in the creation of a recoil electron and photon scattering angle θ, due to the conservation of energy and momentum. The energy of the scattered photon is calculated as

$$h\nu' = \frac{h\nu}{1 + \frac{h\nu}{m_0 c^2}\left(1 - \cos(\theta)\right)}, \tag{3.1.2.1}$$

where h is Planck constant, ν is initial and ν' consequential frequency of photon, $m_0 c^2$ is a rest–mass energy of electron. Since all scattering angles are possible, the energy range of secondary photons is also wide. [16]

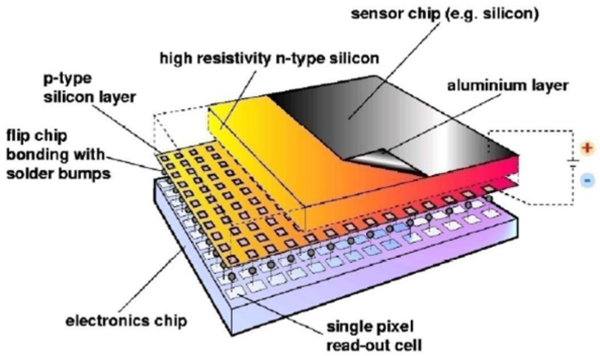

Figure 3.3: Cross-section of a hybrid pixel detector [17].

3.1.3 Electron–positron pair creation

Having at least twice the rest–mass of electron $E_0 = 1.02$ MeV, energy of photon is converted into an electron–positron pair, all excess energy above this threshold is preserved as a kinetic energy of created particles. This reaction is more plausible for large energies of incoming photons of the order of MeV.

3.2 Medipix2

Medipix2 is a hybrid pixel detector primarily designed for photon-counting X-ray imaging. It was developed by the Medipix collaboration which is part of the European Organization for Nuclear Research (CERN) The single chip has 256×256 pixels with size $55 \times 55\ \mu\mathrm{m}^2$, larger coverage area can be achieved by combination of 4 chips as is shown in the figure 3.4a, this configuration is called "quad". [17]

3.2.1 Readout

Because of the need for a new and flexible interface, a CoaXPress readout has been developed. It serves as an interface between the detector and a computer, ensuring proper operation and data streaming. Its main advantage is a usage of a coaxial cable between setup and computer, which provides around 100 Hz operation - maximum for the Medipix2 chip. The dead time needed for the detector to process the signal and transfer data is 9.2 ms. Framerate therefore depends on the width of an acquisition window.

3.2.2 Software

As a mean of controlling the setup from computer, Adapted Software for PIxel REadout (ASPIRE) has been developed. It provides facilities for the detector calibration, data storing and further processing.

One of the important panels for usage is Digital to Analog Converter (DAC). By changing the values, different voltage levels are set in the electronic circuit, modifying the response of amplifier, adjusting the low threshold (THL) and more.

3.2.3 Equalization

One of the important functions of the software is equalizing pixel response. Since each pixel is a stand-alone unit, due to minor differences during production a set THL can

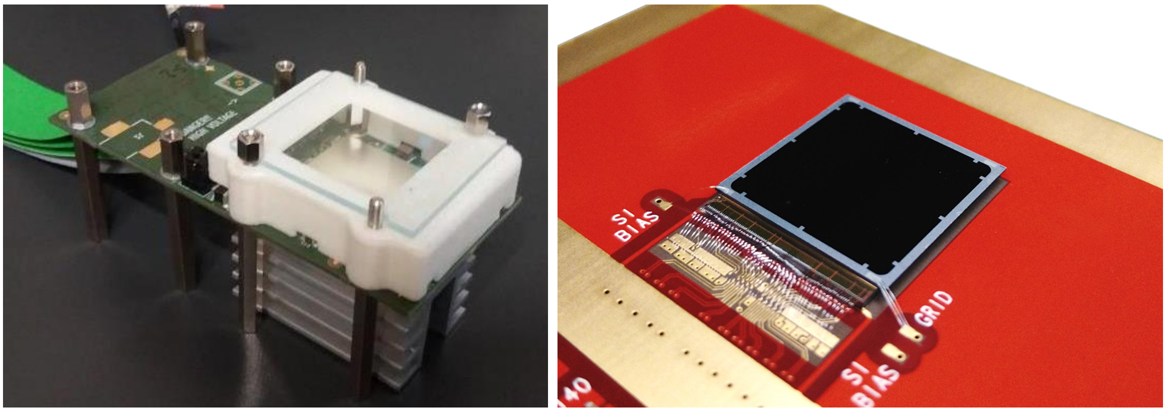

(a) Medipix2 detector. (b) Timepix3 detector.

Figure 3.4: Used semiconductor pixel detectors.

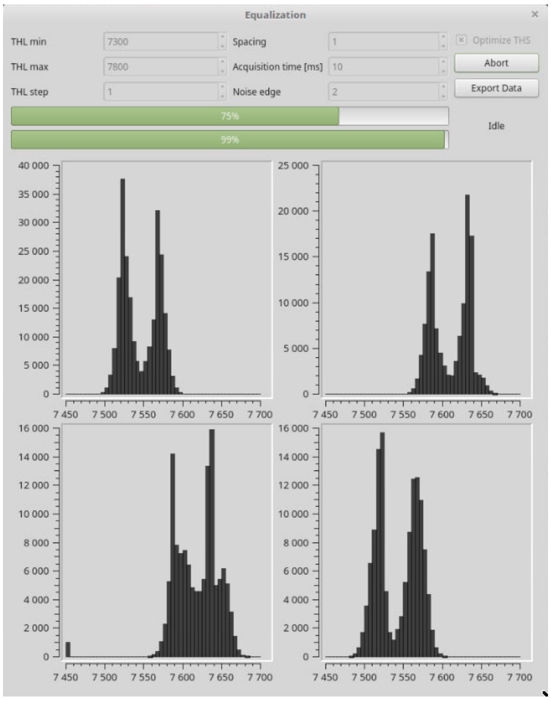

Figure 3.5: Finished equalization of Medipix2 Quad detector. Histograms represent number of pixels that reached noise edge depending on THL, for each chip. [18]

have different effect in each pixel. Therefore 3 low bits in each pixel DAC exist, enabling fine tuning of the response.

ASPIRE solves this inequality during a procedure in which all the pixels are monitored according to the different threshold setting. After starting the procedure, a specified range of the detector THL is scanned for two different values of low local bits - all set as zeros and ones. By doing so, the response to the noise edge of each individual pixel is gained at different THL value, which is stored.

The algorithm then calculates the best possible combination for bit values using the equations

$$\mathrm{adj}_{ij} = 7 - \left[\frac{\mathrm{THL}_{ij} - \mu_{\min}}{\mu_{\max} - \mu_{\min}}\right], \text{and} \quad \mathrm{adj}_{ij} = \left[\frac{\mu_{\max} - \mathrm{THL}_{ij}}{\mu_{\max} - \mu_{\min}}\right] \tag{3.2.3.1}$$

where $\mu_{\max}$, $\mu_{\min}$ are means of the low and max distributions and is THL_{ij} is THL value

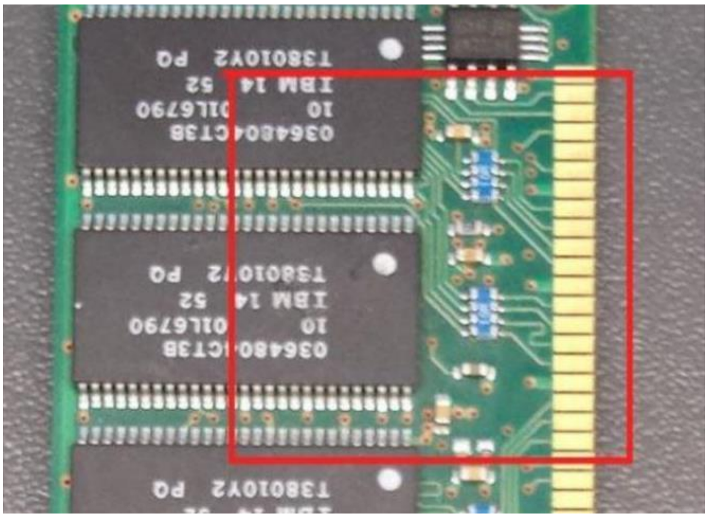

(a) Image of RAM.

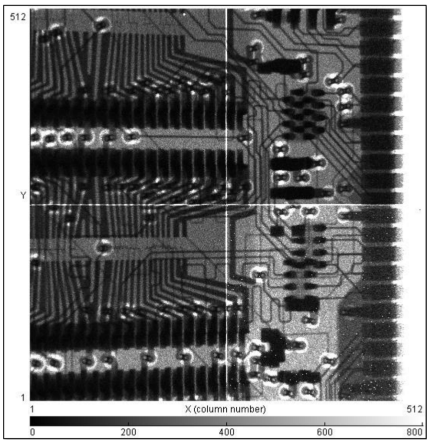

(b) Without equalization.

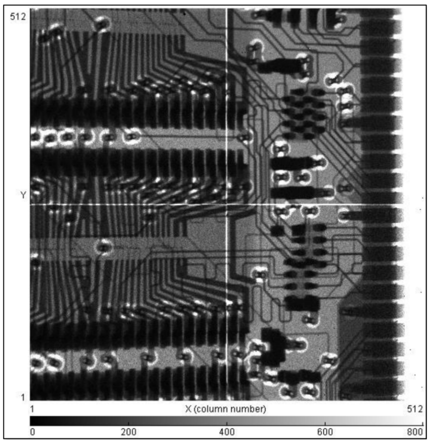

(c) With equalization.

Figure 3.6: Equalization effect on usage of Medipix2 quad detector. Image of RAM with and without equalization. Noise is distinctly larger in the figure without equalization, this can be seen the most easily in the lower right chip of both quad sensors.

at which the pixel reached the noise level. The result is then averaged. The output value for each pixel is between 0 and 7 and set as low local bits value. Finished equalization for Medipix2 Quad is in the figure 3.6. [18]

The resulting effect of the equalization is in the figure 3.6.

3.3 Timepix3

Similarly to Medipix2, Timepix3 is an ASIC developed by CERN collaboration, it has 256×256 pixels with size 55×55 µm^2. It is a newer version, with a bit different functionality. Timepix detectors are mainly used for acquiring timing information – time of arrival (ToA) and time over threshold (ToT), with the latter providing energy deposition information.

The main difference of version 3 is simultaneous recording of ToT and ToA, in addition to a so-called data driven mode – pixels send the signal only when detected. This enables the detector to stay sensitive most of the time.

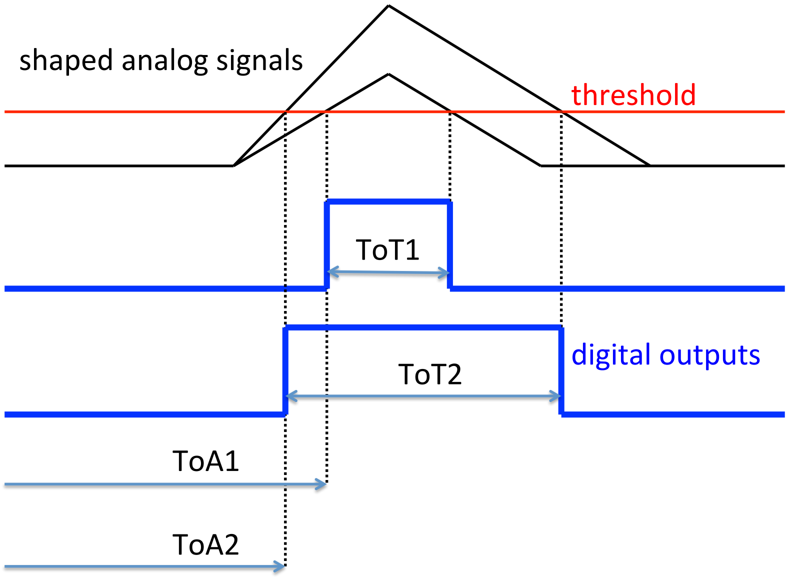

Figure 3.7: Signals have similar rise time, therefore larger ones cross THL earlier, resulting in earlier ToA. [20]

3.3.1 Readout

NIKHEF developed a general purpose readout system called SPIDR, which can also accept and time stamp an external trigger pulse. Packets of information are sent via ethernet cable in 64 bit bunches. Maximal transfer rate is 80 MPix/s. [19]

3.3.2 Calibration

The calibration of the device was done by the author of this work on velocity mapping experiment. [20] A laser interacts with molecule which breaks to ions and electrons, which are then accelerated towards the phosphorus screen and are converted to light. That signal is recorded by Timepix3Cam (device with lenses, Timepix3 chip and sensor which interacts with visible light).

Since the shape of the analog signal corresponds to the energy, a time-walk effect occurs for the measured data. This effect is best described in the figure 3.7 As the rise time is similar for all energies, the interactions that occured at the same time are registered with different ToA. Difference in the ToT then enables correction of such effects.

The calibration was therefore made using correlation of ToF (ToF = ToA - trigger time) and ToT, together with centroiding, as interaction of light from both electrons and ions creates clusters in the sensor. Comparison of all corrections are in the plots of ToT vs ToF for electron and double ion peak (CH_2Br+)are in the figure 3.8. The resulting improvement is in the figure 3.9, the sigma of gaussian fit for the double ion peak improved by almost a quarter.

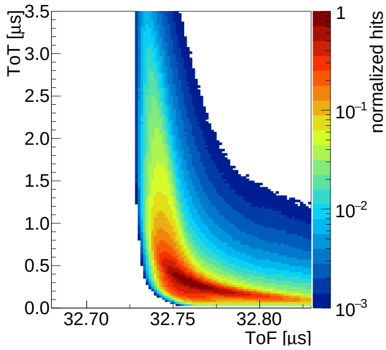

(a) Electrons in raw data.

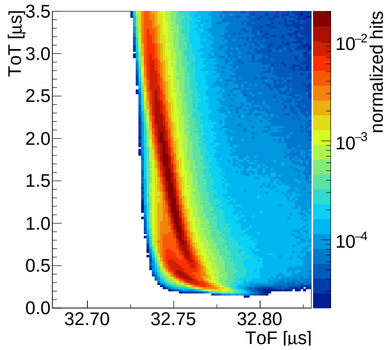

(b) Electrons after centroiding.

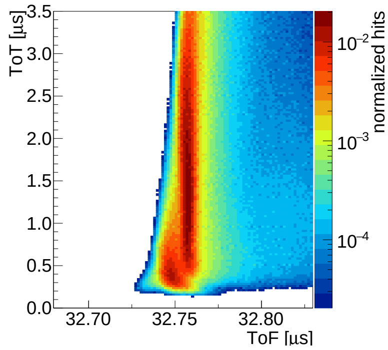

(c) Electrons after centroiding and ToT correction.

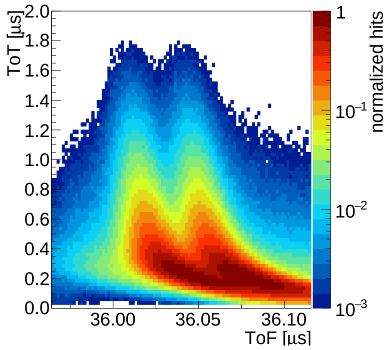

(d) Ions in raw data.

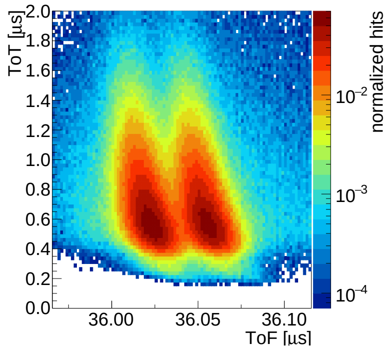

(e) Ions after centroiding.

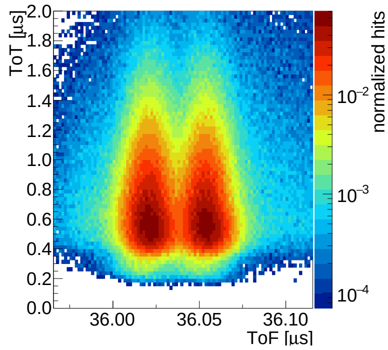

(f) Ions after centroiding and ToT correction.

Figure 3.8: ToT and ToF correlation for electrons and ions before and after centroiding and TOT correction. [20]

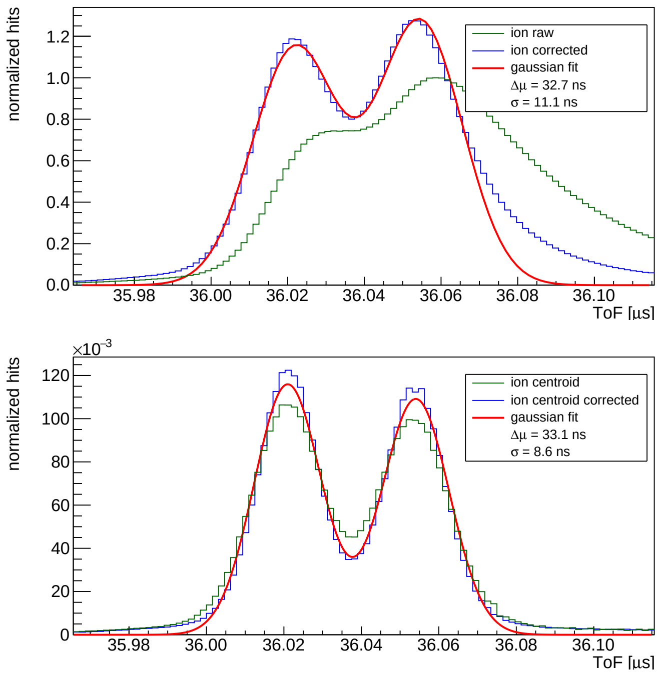

Figure 3.9: Effect of ToT calibration on time resolution. [20] The sigma for the gaussian fit of both peaks improved from 11.1 µs to 8.6 µs.

Chapter 4

Results

Prior to all measurements, the detector has to be equalized in order to ensure the same response of all pixels. The procedure was run on each used detector, using corresponding software.

4.1 PFZ-200

Results of the measurement on PFZ-200 were part of the Bachelor's thesis of the author of this work. [21]

The measurement was done using Timepix detector (), the configuration from the figure 4.1 was used. In addition to it, an aluminium foil was used to cover the pinhole. Acquisition time was $t = 2\,\mathrm{s}$, so as to record the whole discharge.

The data acquired from the measurement are shown in figure (4.2). The addition of the aluminium filter greatly improved the visualisation of the collapse phase of plasma focus, where pinching occurs. The oblong shape in the bottom part of the images is caused by hard X–rays radiated by the central anode where it was hit by the plasma column.

In all the pictures, z–pinch is clearly seen. Hints of instabilities are probably also visible in the measured data.

Those measurements proved that it is possible to use such configuration to obtain reasonable results. However, the data could not be compared to the measurement from MCP, due to technical difficulties with the device, at the time of the measurement.

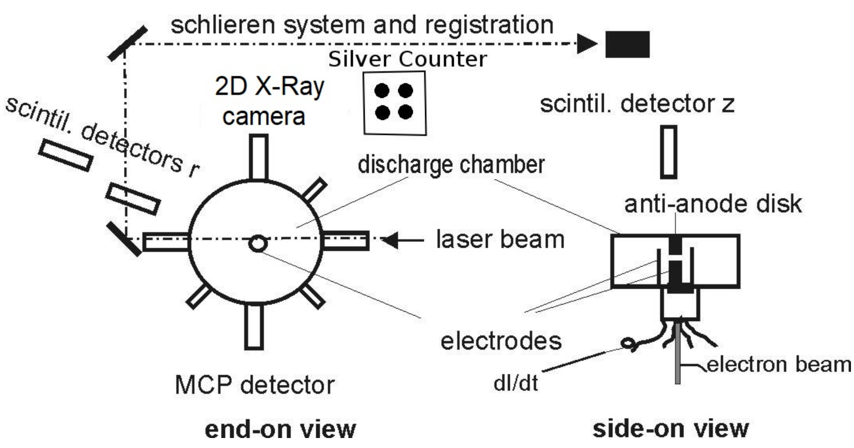

Figure 4.1: Types of diagnostics at PFZ-200. Medipix2 is stated as a 2D X-ray camera.

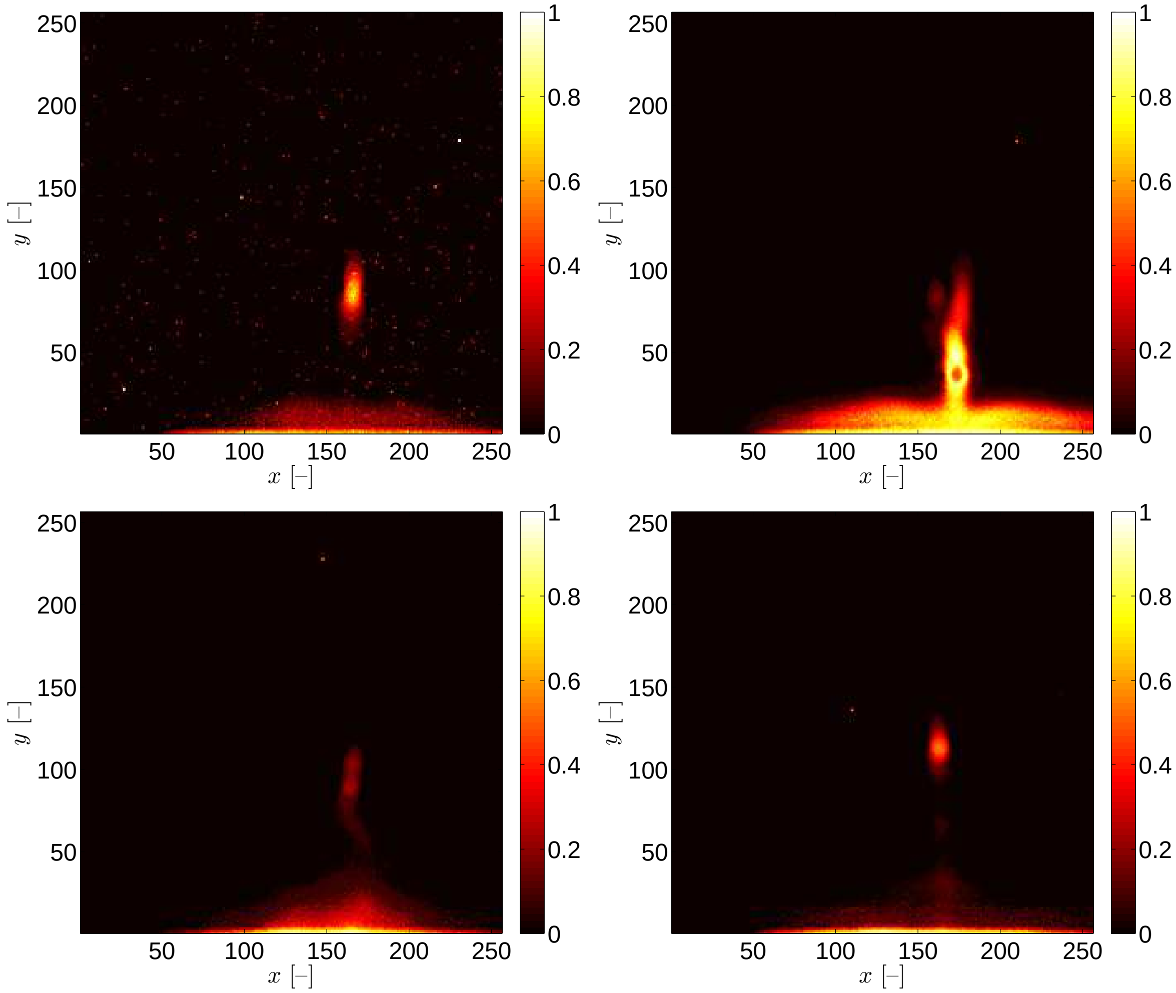

Figure 4.2: Different discharges from plasma focus PFZ-200 taken by Timepix detector, covered by aluminium foil. Possible structures similar to instabilities or hotspots are present. Data are taken in ToT mode, normalized to maximal value. [21]

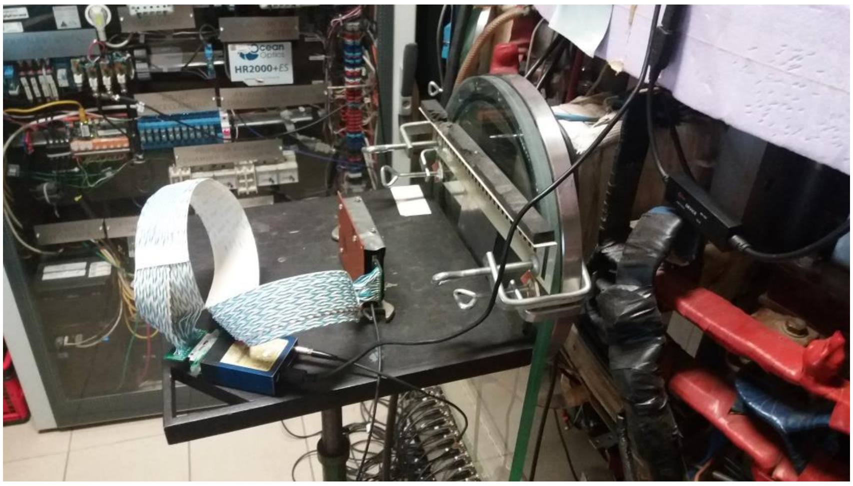

Figure 4.3: Detector setup at tokamak GOLEM.

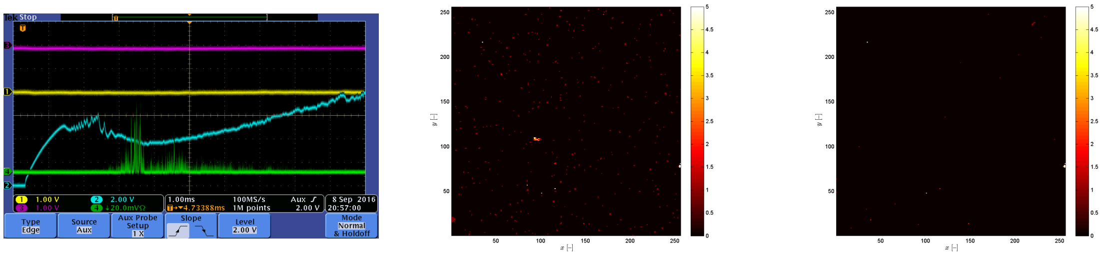

(a) Oscilloscope signal, channel 4 represents scintillator.

(b) Medipix2 data, taken during discharge.

(c) Medipix2 data, taken after discharge.

Figure 4.4: Data from discharge 22207. Medipix2 (covered by leaded pinhole) had acquisition time set to 10 s in order for the detector to be sensitive during discharge. Empty frame right after the discharge for comparison, together with data from scintillator.

4.2 GOLEM

The main purpose of the measurements at tokamak GOLEM was to test the capabilities of Medipix2 to detect ionizing radiation which is normally detected by scintillator detector. A simple setup with lead pinhole was created and positioned close to the tokamak, shown in the figure 4.3.

Different positions were tested, all with similar results. When the tokamak was in regime for RE generation (according to [22]), Medipix2 detected radiation, even though it was placed behind the thick glass plate. Results are in the figure 4.4.

One of the issues at GOLEM were acquisition frequency. As the maximal rate for Medipix2 is 100 Hz, during the standard tokamak shot (lasting 20 ms) up to 2 frames could be made, with acquisition window of only 1 ms. However, the results indicate that semiconductor detectors could be used for the measurements of the RE disruptions.

4.3 COMPASS

Medipix2 was part of two RE campaigns at tokamak COMPASS. Since the typical discharge lasts hundreds of ms, maximal acquisition rate of the detector was necessary in order to monitor temporal development of RE. For this purpose, the first campaign was

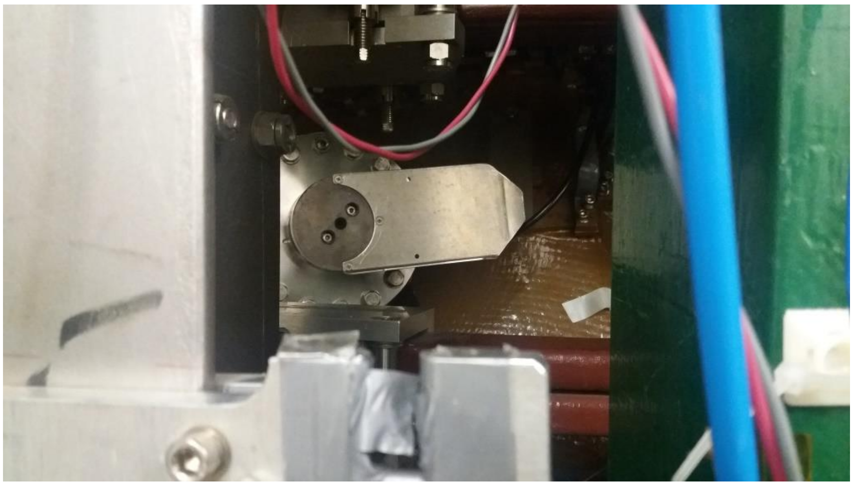

Figure 4.5: Pinhole setup at tokamak COMPASS.

mainly used for testing the newly developed CoaXPress readout and ASPIRE software. In order to obtain higher spatial resolution, quad setup (combination of four chips) was used.

The detector was attached to a 1 cm thick lead pinhole, connected to a side port at tokamak, see figure 4.5. The port was covered with a beryllium, glass which together with pinhole, provide geometrical optics system with sufficient resolution of a part of the inner side of the vacuum vessel.

Acquisition was always triggered, however, the trigger source was frequently changed in between the shots due to problems with receiving the signal. Additionally, trigger repetition had to be used, sending 10 signals during 1 ms.

4.3.1 Campaign 1

The first RE campaing with the usage of Medipix2 detector and CoaXPress readout was at the end of 2016 - 9th to 20th of December.

Position of the detector, together with other diagnostic types, is shown in the figure 4.6. Due to the positioning, the detector was unable to obtain any data showing spatially–relevant information, which could be caused by the wrong orientation in respect to the vacuum vessel.

The results from couple of successful shots are in the figure 4.7, where histograms from Medipix2 are compared to X–ray data from a scintillator and from a photo-neutron detector. The data analysis showed promising results in the respect of correlation of Medipix2 data and acquired X-ray intensities, as well as flux of photo-neutrons during the end of the discharge.

It was also found that such high energies of incident X–rays produce high number of scattered electrons from the pinhole, which were observed in the detector. Therefore additional aluminium shielding was added for the purposes of the next campaign.

4.3.2 Campaign 2

The second campaing with Medipix2 and CoaXPress readout was in the middle of 2017 - 12th to 23rd of June.

Position of the detector, together with other diagnostic types, is shown in the figure 4.8. The CAD image of the used port is in the figure 4.9, using the same configuration as in

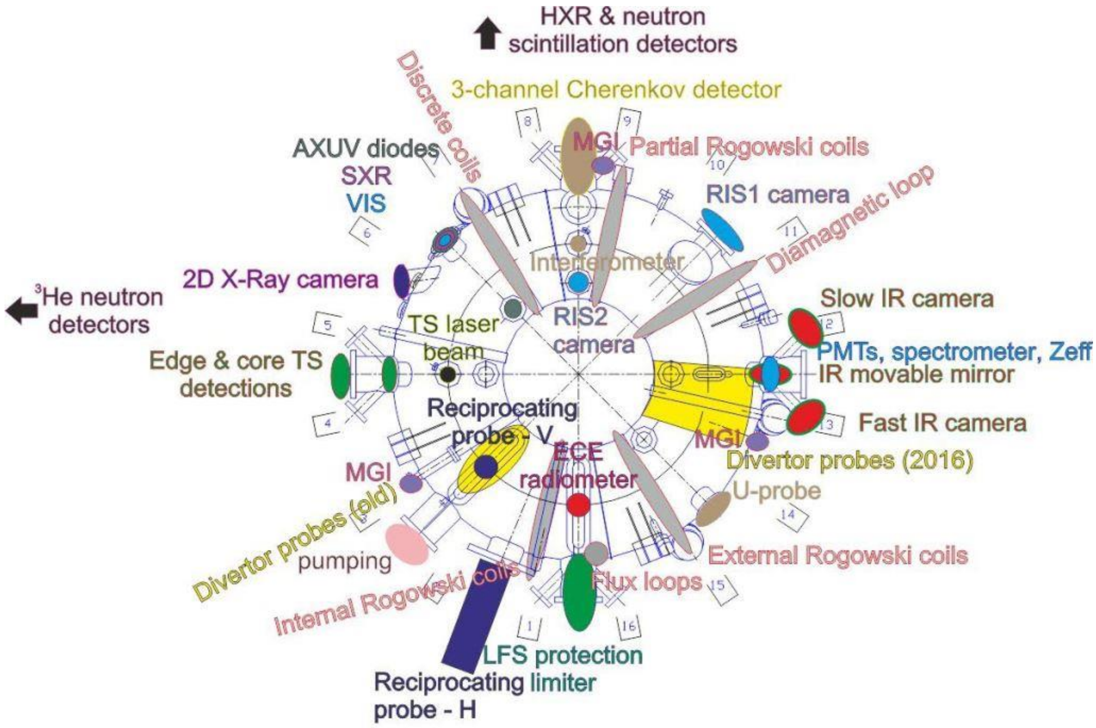

Figure 4.6: Types of diagnostics during RE campaign. Medipix2 is stated as a 2D X-ray camera on the left side.

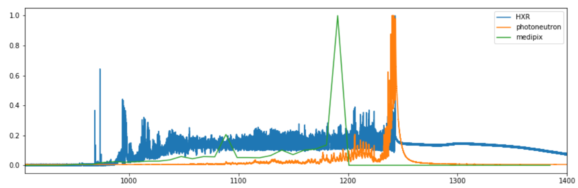

(a) Shot 13091.

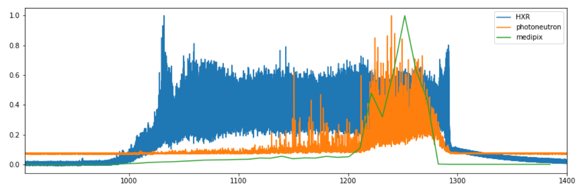

(b) Shot 13091.

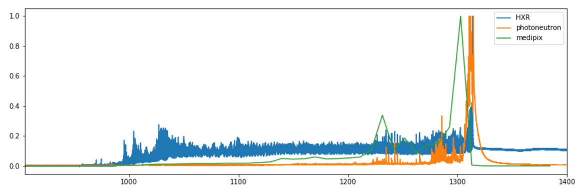

(c) Shot 13091.

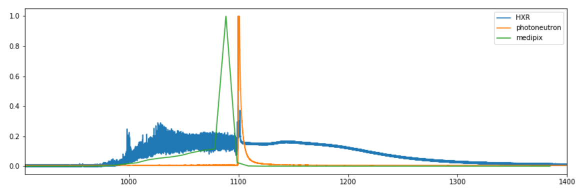

(d) Shot 13091.

Figure 4.7: Time development of X–ray flux measured by Medipix2, scintillator and photo-neutron counter. Time stamping of the Medipix2 is 10.2 ms (1 ms acquisition and 9.2 ms dead time). Time axis is in ms, each dataset is normalized to its maximal value.

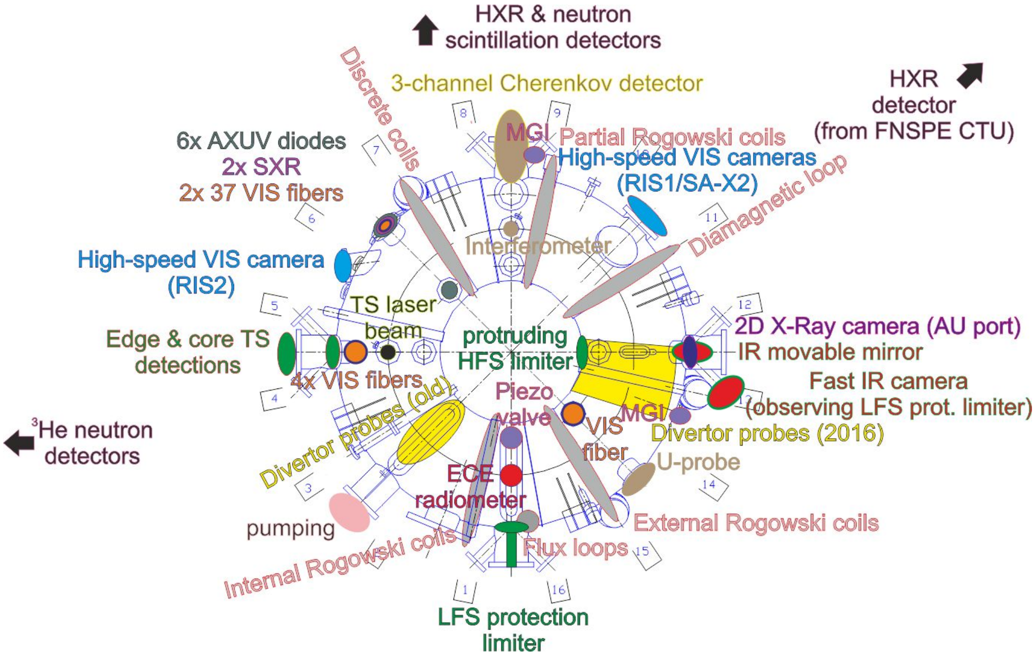

Figure 4.8: Types of diagnostics during RE campaign. Medipix2 is stated as a 2D X-ray camera on the right side.

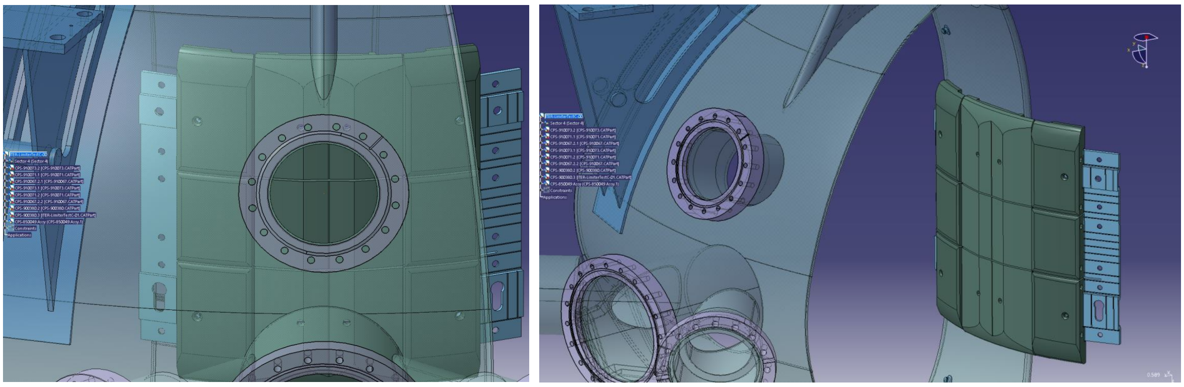

(a) Perpendicular view to the port.

(b) Side view of the setup.

Figure 4.9: CAD model of used port during second COMPASS campaign. Distance between the attached pinhole to the upper port is 50 cm, distance between the pinhole and the detector is 0.5 cm.

the previous campaign - only with addition of aluminium foil and additional shielding all around the detector setup. As is clearly visible from the figures, geometric configuration was chosen in order to observe part of the HFS limiter.

Similarly to the previous experiments, an analysis of temporal evolution of signal from Medipix2, scintillator and photo–neutron counter was made. The sum of the pixelated semiconductor detector signal is comparable to other diagnostics in most of the shots. The offsets could be caused by wrong stating of the trigger time during the analysis. Results are shown in the figure 4.10.

In addition to previous measurements, experiments with vertical positioning of the plasma column were performed. This was observed as a larger signal in a cluster on the detector, changing position with the time. Results are in the figure 4.11. Data from the y–axis histograms and of the frames show change of the position about 30 pixels during 20.4 ms.

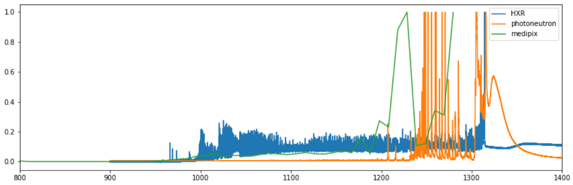

(a) Shot 14494.

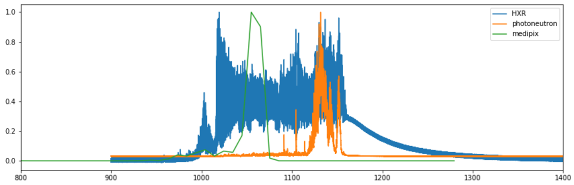

(b) Shot 14495.

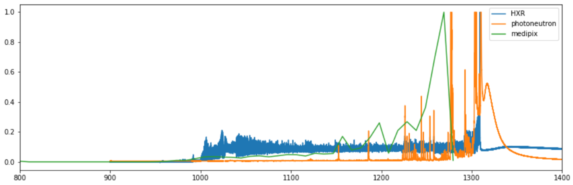

(c) Shot 14509.

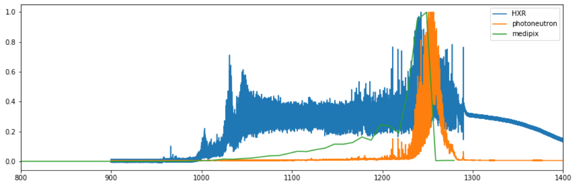

(d) Shot 14513.

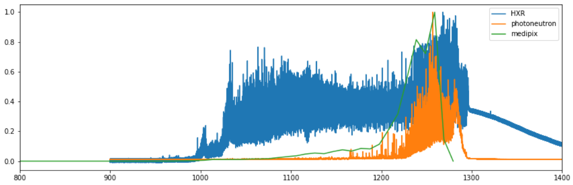

(e) Shot 14517.

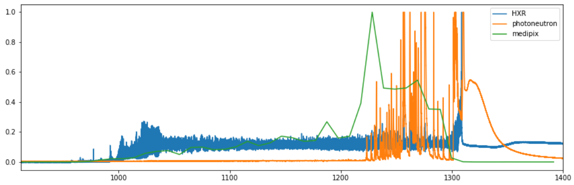

(f) Shot 14553.

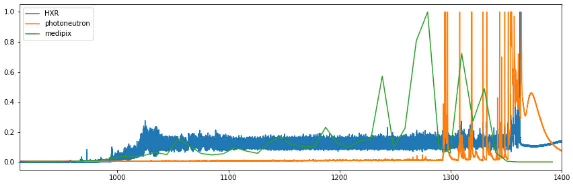

(g) Shot 14557.

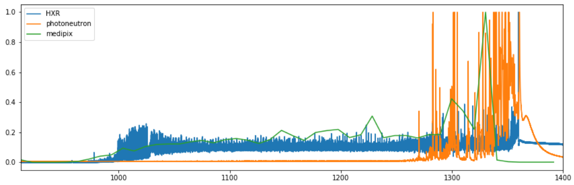

(h) Shot 14555.

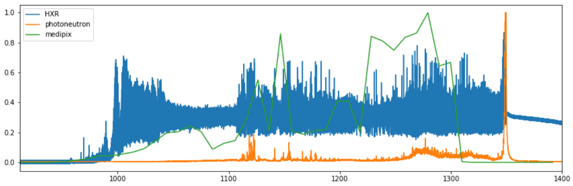

(i) Shot 14557.

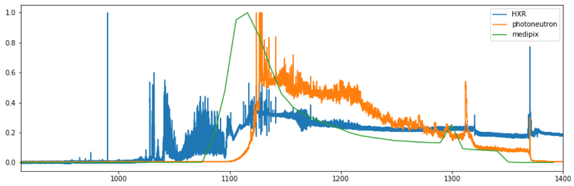

(j) Shot 14599.

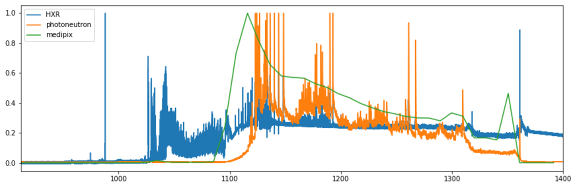

(k) Shot 14601.

Figure 4.10: Time development of X–ray flux measured by Medipix2, scintillator and photo-neutron counter. Time stamping of the Medipix2 is 10.2 ms (1 ms acquisition and 9.2 ms dead time). Time axis is in ms

During one of the last discharges, an interesting time–development of a spatial signal was observed, shown in the figure 4.12. The effect can be monitored in the lower left part of the quad detector, in which a clear change of the signal is visible. Since the interpretation of such effect is not possible without fully understanding the geometry, Geant4 simulation of the tokamak should be performed and analyzed. So far, the only viable statement is that the signal is not a detector defect, as the hit–rate reaches less than 10 % of the maximal value and does not show typical effects of the lost configuration.

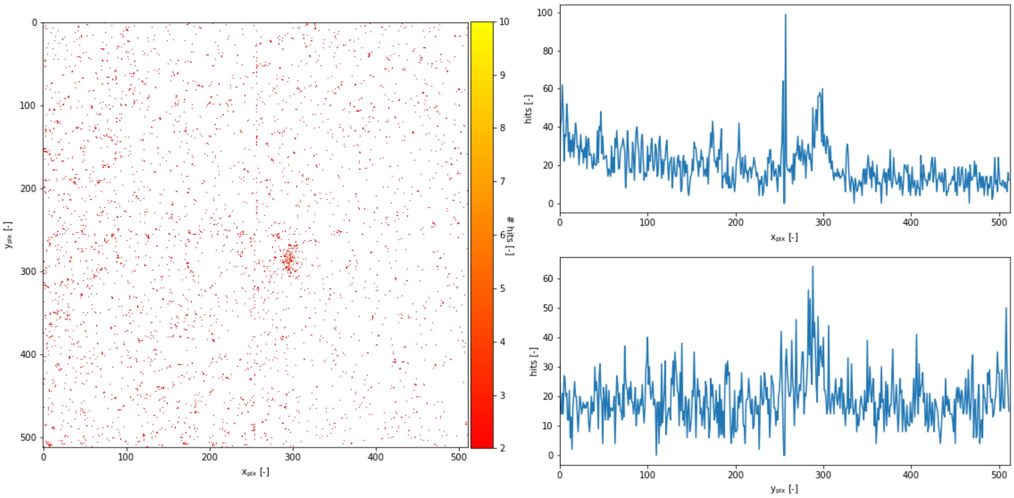

(a) $t = 1014.0\,\mathrm{ms}$.

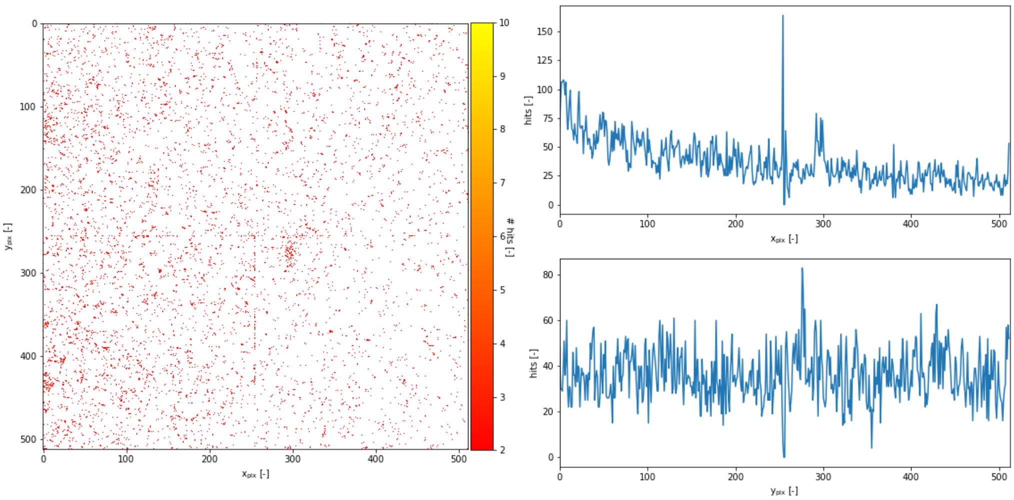

(b) $t = 1024.2\,\mathrm{ms}$.

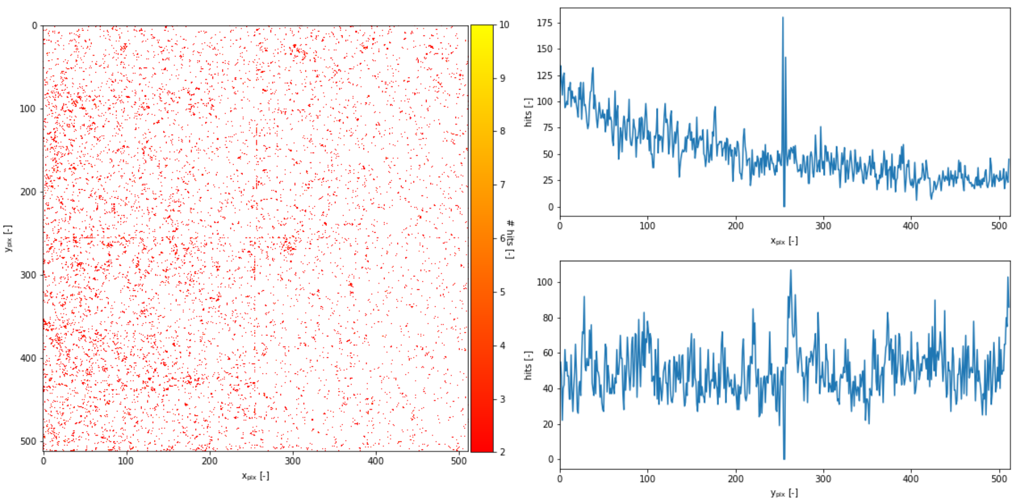

(c) $t = 1034.4\,\mathrm{ms}$.

Figure 4.11: Data from Medipix2 during shot 14555. Masked values above 10 and below 2, masked middle cross (different pixel configuration on the sides close to other chips). Visible positioning of plasma on limiter is observed on y–axis (from pixel 300 in upper figure, to 270 in lower figure, during 20.4 ms).

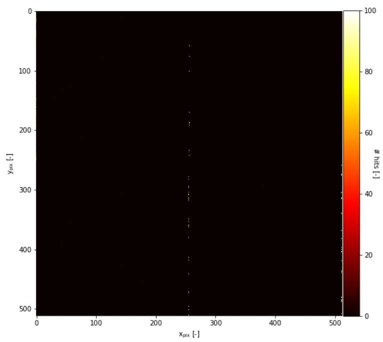

(a) $t = 1075.2\,\mathrm{ms}$.

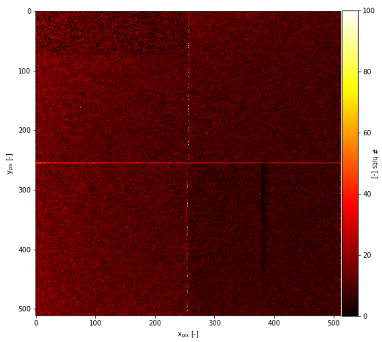

(b) $t = 1085.4\,\mathrm{ms}$.

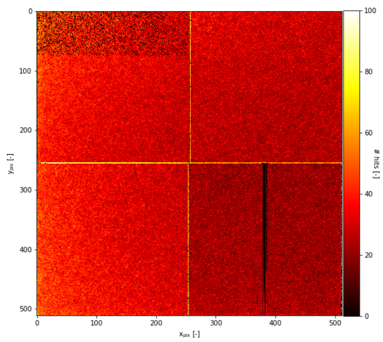

(c) $t = 1095.6\,\mathrm{ms}$.

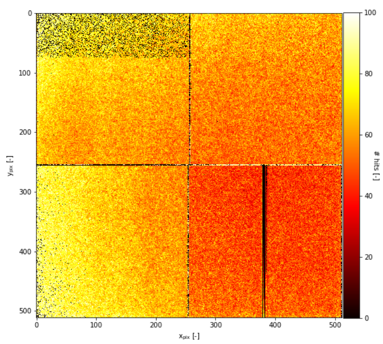

(d) $t = 1105.8\,\mathrm{ms}$.

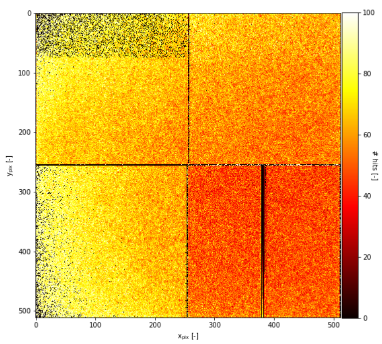

(e) $t = 1116.0\,\mathrm{ms}$.

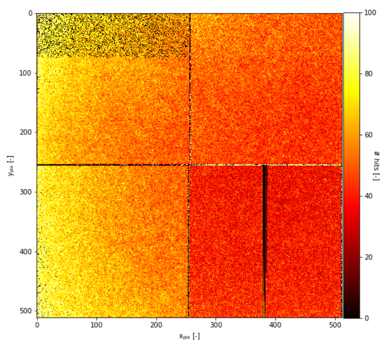

(f) $t = 1126.2\,\mathrm{ms}$.

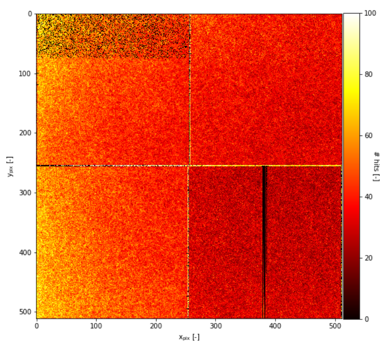

(g) $t = 1136.4\,\mathrm{ms}$.

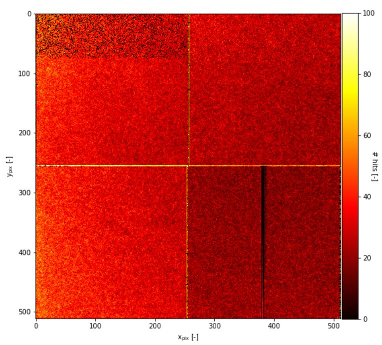

(h) $t = 1146.6\,\mathrm{ms}$.

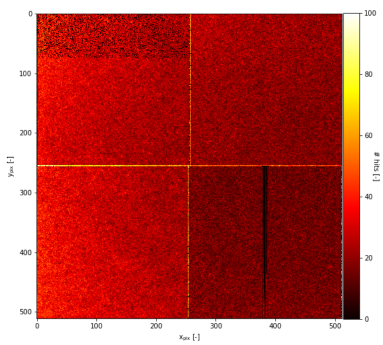

(i) $t = 1156.8\,\mathrm{ms}$.

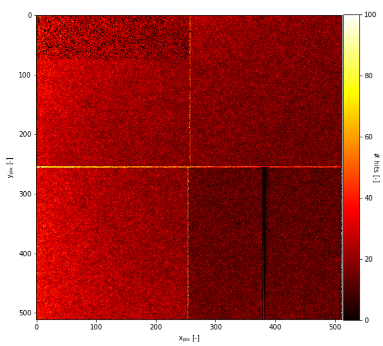

(j) $t = 1167.0\,\mathrm{ms}$.

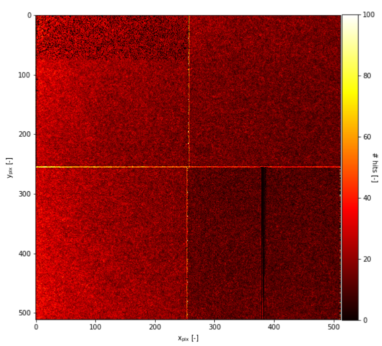

(k) $t = 1177.2\,\mathrm{ms}$.

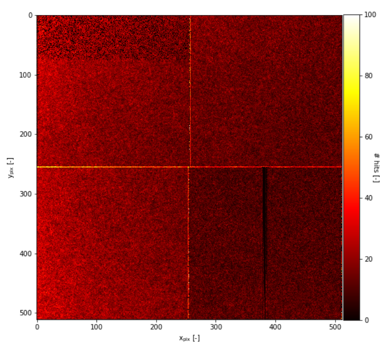

(l) $t = 1187.4\,\mathrm{ms}$.

Figure 4.12: Temporal development of signal from Medipix2 during shot 14599. Visible change of spatial position of the signal in dependent on the time. Masked values above 100, part of upper left chip with bad configuration, THL in lower right set to different value.

Chapter 5

Conclusions

Semiconductor pixel detectors proved to be a great addition to the diagnostic methods of different fusion experiments. Since their full potential in this field of research is still not fully exploited, the application should be furtherly studied. Application of such detectors could be developed as a new method of diagnostics, providing both spatial and temporal resolution throughout the plasma discharge.

For devices such as plasma focus, obtaining both energy and exact timing of produced X–rays would help in understanding of the processes that lead to the collapse of an equilibrium. Additionally, possible detection of charged particles or neutrons could be examined.

For the tokamak experiments, it is crucial that the process of RE creation and propagation is well understood as it poses a large threat to instrumentation.

Proper operation of Medipix2 with newly developed CoaXPress readout and ASPIRE software was successfully tested. Comparison of the measured data to the other X–ray diagnostics is promising. Moreover, the pixelated detector proved to be able to measure expected spatial information. However, as the flux was large and the energy distribution of the radiation was concentrated on the hard X–ray part of the spectrum, only some of the acquired frames contained relevant information.

For all studied devices, larger frame–rate could be a major improvement, as more interesting data would be obtained. This could be improved by the usage of a newly developed monolithic detector X–chip.

Moreover, Geant4 simulation models of the large parts of the experiments should be devised, and subsequent analysis of the simulations of interactions of gamma and X–rays within the geometrical optics unit and the detector performed. Output of the analysis will be crucial to proper understanding of the behavior of the signal recorded by the semiconductor pixel detectors. Such model could also be utilized for other ionizing radiation diagnostic or for the survey of radiation safety of the area.

Bibliography

[1] J. Wesson and D. Campbell, *Tokamaks.* Oxford university press, 4 ed., 2011.

[2] A. Stahl *et al.*, "Effective critical electric field for runaway-electron generation," *Physical Review Letters*, vol. 144, no. 11, 2015, http://dx.doi.org/10.1103/PhysRevLett.114.115002.

[3] O. Ficker, "Generace, ztraty a diagnostika ubihajicih elektronu v tokamacich," Master's thesis, FNSPE CTU in Prague, 2015.

[4] JET/UKAEA, "2015 Generating runaway electrons in jet to benefit iter," 2015.

[5] T. J. M. Boyd and J. J. Sanderson, *The Physics of Plasmas.* Cambridge university press, 2003.

[6] M. A. Liberman, J. S. de Groot, A. Toor, and R. B. Spielman, *Physics Of High-Density Z-Pinch Plasmas.* Springer, 1999.

[7] P. Kubes *et al.*, "Research of the small plasma focus with an auxiliary electrode at deuterium filling," *Plasma Physics Reports*, vol. 35, no. 10, pp. 824–827, 2009, http://dx.doi.org/10.1134/S1063780X09100031.

[8] M. A. Liberman and A. J. Lichtenberg, *Principles of Plasma Discharges and Materials Processing.* John Wiley & Sons, 2 ed., 2005.

[9] D. L. Willenborg and C. D. Hendricks, *Design and Construction of a Dense Plasma Focus Device.* 1976.

[10] J. Zajac *et al.*, "Power supply system for the compass tokamak re-installed at the ipp, prague," *Fusion Engineering and Design*, vol. 84, pp. 2020–2024, 06 2009, http://dx.doi.org/10.1016/j.fusengdes.2008.11.092.

[11] R. Panek *et al.*, "Status of the compass tokamak and characterization of the first h-mode," *Plasma Phys. Control. Fusion*, vol. 58, 2016.

[12] P. Kulhanek, *Úvod do teorie plazmatu.* AGA, 2014.

[13] J. Braithwaite, "The stability of toroidal fields in stars," *Astronomy & Astrophysics*, vol. 453, no. 2, pp. 687–698, 2006, http://dx.doi.org/10.1051/0004-6361:20041282.

[14] P. Kubes, "Impulsní silnoproudé výboje a jejich diagnostika," 2004.

[15] H. Dreicer, "Electron and ion runaway in fully ionized gas i," *Physical Review*, vol. 115, no. 238, 1959, http://dx.doi.org/10.1029/2004GL019795.

[16] G. F. Knoll, *Radiation Detection and Measurement.* John Wiley & Sons, 4 ed., 2010.

[17] X. Llopart, *Design and characterization of 64K pixels chips working in single photon processing mode.* PhD thesis, Mid Sweden University, 2007.

[18] P. Svihra, "Adapted software for pixel readout - aspire user manual," 12 2016. TACR - FJFI-CK 2016/12.

[19] B. van der Heijden *et al.*, "Spidr, a general-purpose readout system for pixel asics," *Journal of instrumentation*, vol. 12, 2017.

[20] A. Zhao *et al.*, "Coincidence velocity map imaging using tpx3cam, a time stamping optical camera with 1.5 ns timing resolution," *Review of Scientific Instruments*, submitted for publication, https://arxiv.org/abs/1707.06253.

[21] P. Svihra, "Study of thermonuclear plasma using semiconductor detectors," 2015. Bachelor's thesis, FNSPE CTU in Prague.

[22] O. Ficker *et al.*, "Tokamak golem for fusion education - chapter 6," in *42nd EPS Conference on Plasma Physics*, 2015.